Nucleotide excision repair (NER) machinery recruitment by the transcription-repair coupling factor involves unmasking of a conserved intramolecular interface

Alexandra M. Deaconescu[a], Anastasia Sevostyanova[b], Irina Artsimovitch[b], and Nikolaus Grigorieff[a,1]

[a]Howard Hughes Medical Institute, The Rosenstiel Basic Medical Sciences Research Center, Brandeis University, Waltham, MA 02454; and [b]Department of Microbiology, Ohio State University, Columbus, OH 43210

Transcription-coupled DNA repair targets DNA lesions that block progression of elongating RNA polymerases. In bacteria, the transcription-repair coupling factor (TRCF; also known as Mfd) SF2 ATPase recognizes RNA polymerase stalled at a site of DNA damage, removes the enzyme from the DNA, and recruits the Uvr(A)BC nucleotide excision repair machinery via UvrA binding. Previous studies of TRCF revealed a molecular architecture incompatible with UvrA binding, leaving its recruitment mechanism unclear. Here, we examine the UvrA recognition determinants of TRCF using X-ray crystallography of a core TRCF–UvrA complex and probe the conformational flexibility of TRCF in the absence and presence of nucleotides using small-angle X-ray scattering. We demonstrate that the C-terminal domain of TRCF is inhibitory for UvrA binding, but not RNA polymerase release, and show that nucleotide binding induces concerted multidomain motions. Our studies suggest that autoinhibition of UvrA binding in TRCF may be relieved only upon engaging the DNA damage.

cysteine cross-linking | transcription | ATPase stimulation | UvrB

RNA polymerase (RNAP) stalled at DNA lesions on the transcribed strand elicits a preferential pathway for nucleotide excision repair (NER) called transcription-coupled repair (TCR), which is present in Bacteria and Eukarya (1). Bacterial transcription-repair coupling factor (TRCF; also known as Mfd) orchestrates this process by specific recognition of the transcription and NER assemblies, which reflects its twofold role. First, TRCF relieves transcription-dependent NER inhibition due to occlusion of the DNA lesion by RNAP (2). TRCF, an SF2 ATPase with dsDNA translocase but no helicase activity (3), approaches the stalled RNAP from behind and induces its forward translocation by stepping on dsDNA using ATP hydrolysis (4, 5). The consequent collapse of the upstream end of the transcription bubble leads to massive destabilization of the otherwise stable ternary elongation complex (TEC) and transcription termination (4–7). Rho, the only other known bacterial enzymatic terminator, induces termination by a similar forward-translocation mechanism, but translocates along the nascent RNA (8). Second, TRCF recruits the Uvr(A)BC endonuclease to the unmasked lesion by binding to UvrA (4, 9). This initiates a cascade of events resulting in lesion excision and gap filling (4, 10). TRCF also has roles beyond TCR—in the rescue of replication forks stalled by head-on collisions with RNAPs (11), in the development of antibiotic resistance (12, 13), recombination (14, 15), and transcriptional regulation (16, 17).

The crystal structure of apo TRCF (18) revealed a multimodular enzyme with eight domains connected by flexible linkers (Fig. 1A), an architecture that appears primed for large conformational changes, which are believed to be critical for coupling RNAP recognition to recruitment of NER enzymes. Domains D1 and D2 of TRCF are similar to the NER protein UvrB, which also binds UvrA (18, 19), suggesting that these domains serve as a platform for UvrA recruitment and possibly as a "clamp" to restrain the ATP-binding translocase domains (D5 and D6, Fig. 1A), explaining the poor ATPase function and TRCF inability to translocate on naked DNA (22).

Our knowledge of the mechanisms for RNAP recognition and Uvr(A)BC recruitment is rudimentary as TCR intermediates could not be detected (23). It was suggested early on that binding of TRCF/UvrB to UvrA may be competitive (4), but this hypothesis was not addressed subsequently. In addition, a structural model for ATP-bound TRCF (the state that binds DNA) is lacking, leaving details of how this "coupling" occurs unknown. However, it has been previously hypothesized, largely on the basis of in vitro studies carried out without a stalled TEC and UvrA, that the coupling occurs via a single TEC-induced conformational switch within TRCF, which synchronously enables forward translocation and UvrA recruitment (22, 24).

To better understand the mechanism of NER machinery recruitment, we combined functional studies with X-ray crystallography of a core TRCF–UvrA complex and SAXS analysis of TRCF. We show that, in apo TRCF, the UvrA-binding surface is occluded due to intramolecular contacts with domain D7 and that D7 is mobile during the catalytic cycle, but that its mobility is not important for RNAP release. Our data reveal the conformational flexibility of this macromolecular motor during the ATP hydrolysis cycle and details of TRCF mimicry of UvrB in binding to their common partner UvrA; at the same time, our data suggest that TCR relies on a fine temporal and contextual regulation of the various TRCF activities.

Results

TRCF and UvrB Share the Same Mode of UvrA Recognition. Recent studies suggest that domain D2 of TRCF interacts with an UvrA fragment encompassing residues 131–250 (9, 18, 20, 22, 25). Furthermore, the UvrB-homology module (residues 1–349, including D2) as well as residues 131–248 of UvrA were shown to be essential for repair of the template strand in vitro and in vivo without being required for RNAP displacement (21). We have thus designed a minimal TRCF construct, TRCF-Trunc (residues 127–213, Fig. 1), which forms a core TRCF/UvrA complex in the presence of UvrA-Trunc (residues 131–250) as revealed by pull-down assays (Fig. S1A). We then determined the crystal structure of this minimal TRCF-UvrA complex, TRCF-Trunc/UvrA-Trunc (Fig. 1B and Table S1), at 2.8 Å resolution. The model was refined to R/R_{free} of 23.8%/28.2%. Comparison of the two copies of the complex in the asymmetric unit did not reveal any major conformational differences (rmsd$_{TRCF-Trunc}$ = 0.64 Å; rmsd$_{UvrA-Trunc}$ = 0.53 Å).
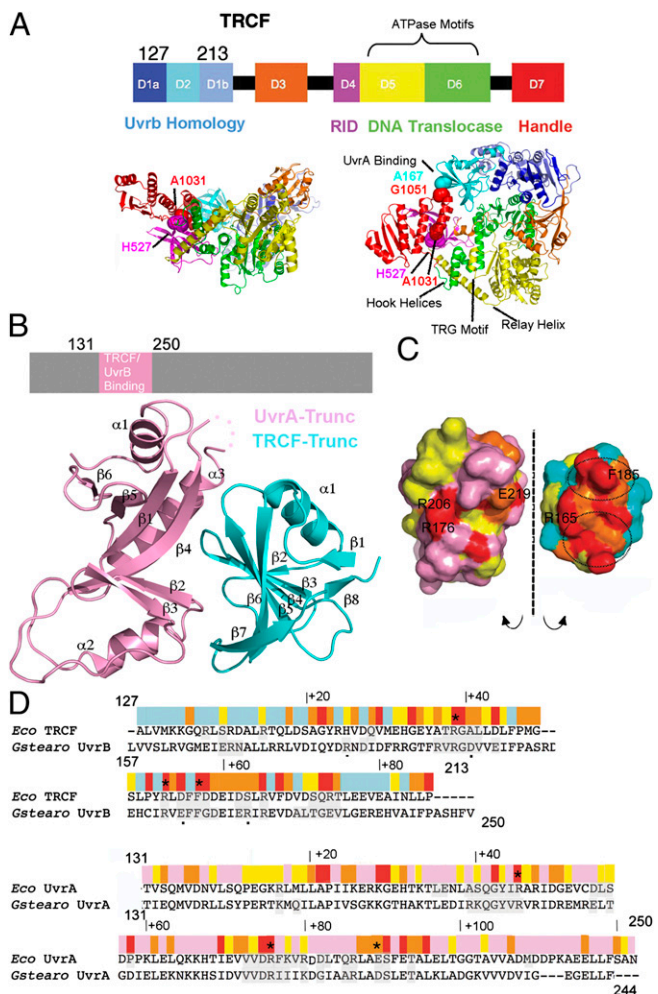
CELL BIOLOGY

Fig. 1. X-ray structure of the *Escherichia coli* TRCF–Trunc/UvrA–Trunc complex. (*A*) Structure of apo *E. coli* TRCF (PDB ID 2EYQ). Location of engineered Cys is indicated by spheres. (*B*) TRCF–UvrA core complex. (*C*) Solvent-accessible surface of the TRCF–UvrA complex, obtained by splaying the complex open and colored by evolutionary conservation as in *D*. (*D*) *E. coli* TRCF-Trunc/*Geobacillus stearothermophilus* UvrB sequence alignment with substitutions affecting UvrA binding (20, 27) marked by an asterisk in TRCF-Trunc and by a small black dot in UvrB. Sequence conservation is indicated with a color ramp from red (invariant) to cyan (variable). Interfacing residues in the TRCF–UvrA and UvrB–UvrA core complexes (20) are shaded in gray. The UvrA sequence is annotated similarly.

Overall, the structure of the core UvrA–TRCF complex is similar to that of the core UvrA–UvrB complex [with 29% sequence identity between TRCF/UvrB and an rmsd of 2.5 Å over the entire backbone of Protein Data Bank (PDB) ID 3FPN] (Fig. S1*B*), pointing to a common mode of UvrA recognition. Interface residues are conserved between UvrB and TRCF (Fig. 1 *C* and *D*), suggesting that TRCF and UvrB binding to UvrA are mutually exclusive. In addition, severe steric clashes occur between UvrA-Trunc and D7 of TRCF (Figs. 1*A* and 2*A*). The unusual TRCF–UvrA interface is punctuated by multiple arginines (Fig. 2*B*) and buries a surface area of 1,796 Å^2, which in the TRCF crystal structure is partially occluded due to intramolecular packing against conserved residues within D7 (Fig. 2*A*), specifically E1045, D1048, and R1049. Binding of UvrA to TRCF could not be detected by gel filtration (4), although an interaction could be detected by pull-down assays, which more readily capture transient interactions (9). In contrast, UvrB binding to UvrA is clearly detected by gel filtration (20). These previous results are in agreement with the small but conserved
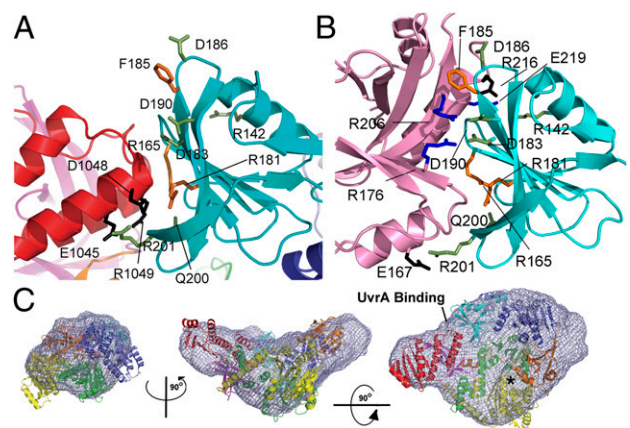

Fig. 2. TRCF autoinhibition of UvrA binding is mediated by domain D7. (*A*) D2–D7 interaction seen in the crystal structure of apo TRCF (PDB ID 2EYQ). Conserved D7 residues are shown in black; interacting D2 residues are shown in green. Substitutions of orange residues are functionally important (21). (*B*) TRCF–UvrA interface. Residues in UvrA that bind UvrB are shown in blue (20). Other interacting residues are colored in black or as in *A*. (*C*) Crystal structure of apo *E. coli* TRCF (colored as in Fig. 1*A*) docked into the SAXS envelope. An asterisk indicates the ATP-binding site.

TRCF–UvrA interface that we observe. Given that TRCF participates in diverse processes beyond NER (11–14, 16, 17), its interaction with UvrA would be expected to be transient and restricted to sites of DNA damage.

The TRCF–UvrA interaction is essentially bipartite, with residues in two adjacent patches contributing to binding (Fig. 1*C*). The patch around invariant R165 is completely occluded due to D7 interaction with the central β-sheet of TRCF-Trunc. The patch around invariant F185, which represents about half of the UvrA/TRCF–Trunc interface area, remains solvent-exposed in apo TRCF, but packs tightly against strand β4 of the central UvrA-Trunc β-sheet (Figs. 1*B* and 2*B*). A triple mutant carrying the R165A R181A F185A substitutions, shown in Fig. 2*B*, is defective in patch repair synthesis and does not bind UvrA in a bacterial two-hybrid system (21). Unlike wild-type TRCF, this mutant also fails to inhibit the GTPase activity of UvrA (21), consistent with an impaired interaction with UvrA. These findings strongly corroborate the physiological relevance of the observed interface. Other conserved solvent-exposed residues in TRCF-Trunc contribute to the intramolecular contacts seen in full-length TRCF. UvrA residues interacting with TRCF include conserved E219, which is important for NER (20), as well as invariant R176 and R206, which also map to the interface and are critical for UvrA–UvrB complex formation (Fig. 2*B*) (20). The corollary of our crystallographic study is that, for UvrA to bind, the D2–D7 contacts must be broken during the coupling process either concomitant with or subsequent to TEC binding. The downstream effect of TRCF binding to UvrA may be to promote dissociation of UvrB from UvrA to form the long-lived UvrB–DNA preincision complex that is required for the repair process (4).

TRCF Is Autoinhibited in Solution. The occlusion of the UvrA-binding surface by the D7 domain in the crystal structure of apo TRCF implies that TRCF is autoinhibited for UvrA recruitment in its apo form. However, domain D7 accounts for a large number of crystal contacts (Fig. S1*C*) (6, 18, 26), raising the possibility that the putative inhibitory position of D7 may not be physiological and that, instead, the UvrA-binding surface is exposed as in UvrB (27). We have therefore probed TRCF using SAXS (Fig. 3). To facilitate study of the ATP-bound state, we engineered a mutant carrying the E730Q substitution in the Walker B motif. This substitution abolishes ATP hydrolysis (Fig. 4*A*), but not ATP, DNA, or TEC binding (Fig. S2). However, this noncatalytic TRCF is deficient in RNAP displacement (Fig. 4*B*), which
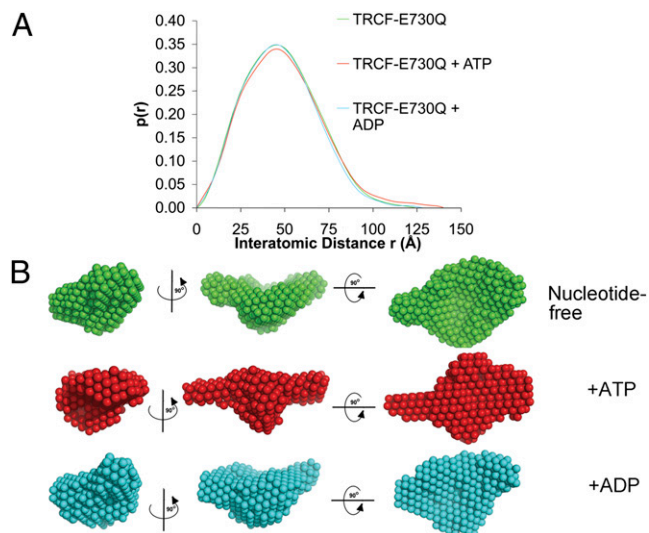
Deaconescu et al.

Fig. 3. Structural flexibility in nucleotide-bound TRCF-E730Q. (A) Pair distribution functions normalized against the area under the curve. (B) Averaged filtered SAXS bead models. Views are as in Fig. 1A.

requires ATP hydrolysis (3, 5). Limited proteolysis confirmed that the conformation of this mutant and the effects of nucleotides on its structure are similar to those of wild-type protein (Fig. S3).

Ab initio shape reconstructions were obtained using GASBOR (28) and then aligned and filtered on the basis of occupancy. The

convergence of the simulations was monitored using the normalized spatial discrepancy (NSD) criterion (29). Models displayed an excellent fit to the experimental data (Fig. S4) and low NSD values (SI Materials and Methods). As shown in Fig. 2C, there is a good fit between the TRCF crystal structure and the solution structure. This rigid-body fit was obtained using an automated exhaustive search starting from a random configuration. The central cavity and D7 "handle" are clearly reflected in the shape of the SAXS envelope. Notably, the relative position of D7 appears unchanged, confirming that TRCF is autoinhibited in solution due to the D2–D7 interaction also observed in the crystal structure. Therefore, for UvrA recruitment to occur, D7 must move to vacate the UvrA-binding site.

Nucleotide Binding and Hydrolysis Reorganize Interdomain Contacts Within TRCF. Given the inhibitory D2–D7 interaction we observe, an important question remains unanswered: What triggers the unmasking of the binding interface and recruitment of UvrA? UvrA recruitment could be triggered by ATP binding and/or hydrolysis. To explore this question, we extended our SAXS analysis to nucleotide-bound TRCF-E730Q. Protein variants remain monomeric irrespective of nucleotide status (Fig. S5), contrasting recent reports of TRCF oligomerizing in other species (30). Comparison of the ab initio models (Fig. 3) and the SAXS-derived parameters R_g and D_{max} (Table S2) revealed closely related conformations for the apo and ADP-bound states, reflecting functional similarities between apo and ADP-bound TRCF, neither of which bind DNA (9). We cannot exclude small-scale differences, especially those affecting the translocase domains that would not be discernible at the resolution of SAXS. When bound to ATP, TRCF appears to adopt a more extended conformation reflected in the longer tail of the model-independent pair distribution function (Fig. 3A). An obvious change involves D7 that appears to swing out into the solvent, thus resulting
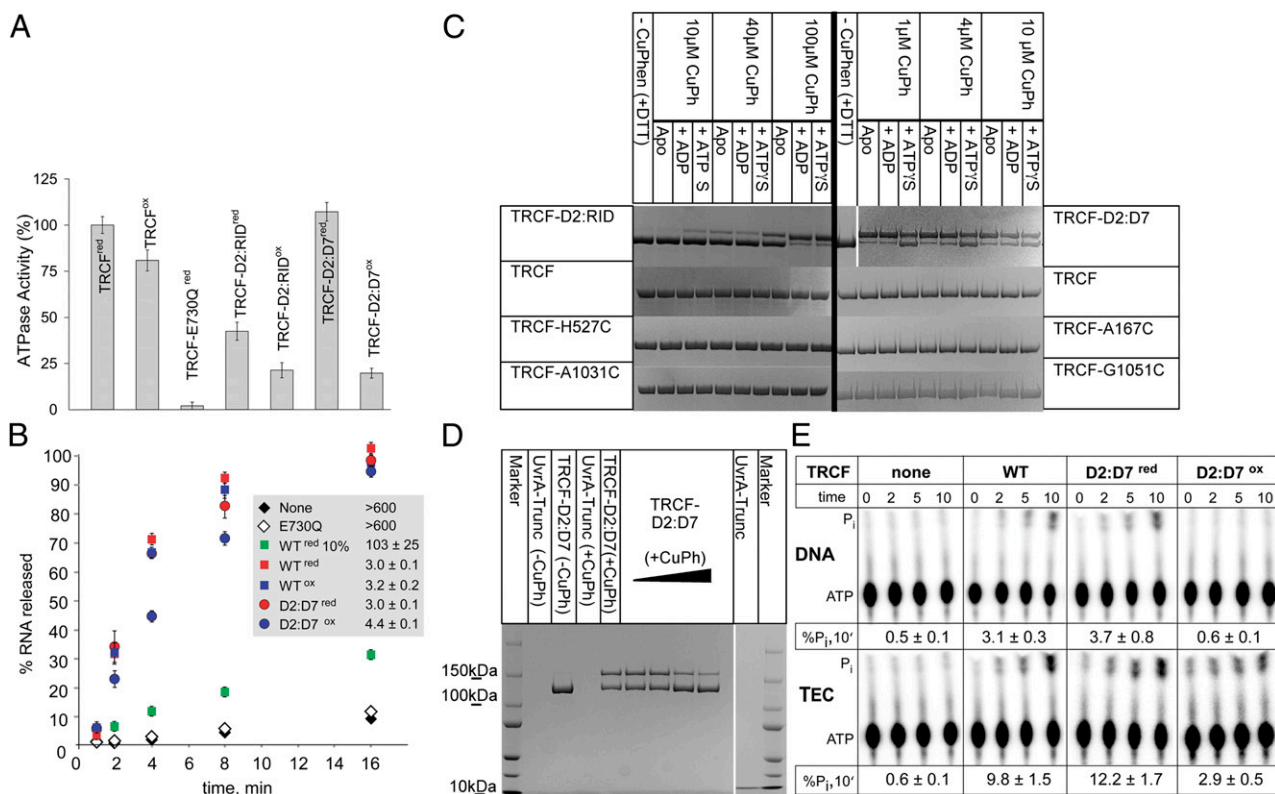
Fig. 4. Characterization of disulfide-locked TRCF variants. (A) Steady-state ATPase activity of TRCF variants under oxidizing ("ox" superscript) and reducing ("red" superscript) conditions. Shown are averages of turnover numbers, k_{cat} (normalized to wild type), obtained from three independent experiments ± SD. (B) Quantification of total RNA released in RNAP displacement assays. TEC half-lives were estimated from three independent experiments and are shown as the average ± SD. (C and D) SDS/PAGE of CuPh-catalyzed disulfide cross-linking with/without ADP/ATPγS (C) and UvrA-Trunc (D). (E) ATP turnover in the presence of DNA template (Upper) and TECs visualized using thin layer chromatography (Lower).

in an increase in D_{max} and a modest change in R_g (Fig. 3B and Table S2). Repositioning of domains D5 and D6 observed in many other ATPases upon ATP binding and/or hydrolysis (31) is also likely to occur. Rearrangements involving the other domains also appear to take place and explain some of the apparent changes in the SAXS envelope, such as a frontal filling of the central cavity in ATP-bound TRCF. The core of the protein, however, remains as compact as in the apo state. To localize structural modules, we have also studied a TRCF variant that lacks domains D1–D3 and has been shown to display elevated ATPase and triplex displacement activity (22), which is repressed in full-length TRCF until binding RNAP (32). To prevent ATP hydrolysis, we introduced the E730Q substitution to generate TRCFΔ(D1-D3)E730Q. Comparison of the SAXS envelopes for TRCF-E730Q and TRCFΔ(D1-D3)E730Q (Fig. S6A) enabled us to assign the central protrusion (present in ATP-bound TRCF-E730Q) and the region diametrically opposed from D7 to the UvrB homology module D1–D2 and the species-specific domain of unknown function D3, respectively.

We also carried out simulations of the ATP-bound state using the coordinates of the Cα backbone of apo TRCF as input in GASBOR. These simulations converged on a solution with an NSD and χ similar to those obtained by ab initio methods. The coordinate-seeded model also features movements of D1–D3 and D7 (Fig. S6B), demonstrating the robustness and re-producibility of the simulated swinging motion of D7 and closure of the central cavity as the core domains rearrange. Placing the apo crystal structure into the SAXS envelope of ATP-bound TRCF using rigid-body fitting revealed significant discrepancies as did the comparison of the scattering profile of crystallized apo TRCF (simulated with CRYSOL) with the experimental SAXS profile of ATP-bound TRCF (Fig. S6C).

To further probe TRCF rearrangements upon ATP binding, we engineered disulfide linkages to reduce the intrinsic flexibility of the protein, lock D7, and hinder exposure of the UvrA-binding surface. We made two sets of substitutions. H527C and A1031C mutations (Fig. 1A) were introduced to create TRCF-D2:RID with a disulfide between D7 and the RNAP interaction domain RID (Fig. 1A and Fig. S1D). The other double mutant (A167C G1051C, TRCF-D2:D7) had an engineered D2–D7 disulfide across the UvrA-binding surface (Fig. 1A and Fig. S1D). Upon purification, disulfide formation became evident from the altered mobility of purified TRCF-D2:RID and TRCF-D2:D7 in SDS/PAGE analyses (Fig. S7A). Treatment with a reducing agent and subsequent alkylation caused reduction and disappearance of the slower migrating species, thus allowing the altered electrophoretic mobility to be attributed to specific Cys cross-linking. Proteins with single Cys substitutions at the aforementioned positions did not form intramolecular disulfide cross-links during their purification (Fig. S7A) or upon catalyzed oxidation (Fig. 4C), implying that the observed disulfides are due to specific linkage of C527 to C1031 and of C167 to C1051, respectively. These cross-linked mutants eluted like monomers from a size-exclusion chromatography column, with profiles comparable to that of wild-type TRCF (Fig. S5), confirming that the observed disulfides are intramolecular rather than intermolecular.

To compare disulfide-bond-formation efficiencies in the presence of ADP and ATPγS, we used a catalyst, Cu(II) (1, 10) phenanthroline (CuPh), which greatly enhances cysteine oxidation by atmospheric oxygen (33). After complete reduction and buffer exchange, we carried out oxidation at different CuPh concentrations. As shown in Fig. 4C, there was significant formation of the C527–C1013 linkage in ATPγS-bound TRCF-D2:RID and less in apo and ADP-bound TRCF-D2:RID, suggesting that the ATP-like state stabilizes D2/RID in a configuration conducive to disulfide bond formation. This trend was reversed with TRCF-D2:D7: the disulfide formed readily in the absence of nucleotide or with ADP, but not with ATPγS. These results are consistent with the TRCF crystal structure, and our SAXS data indicating nucleotide-dependent mobility of D7.

Because cysteines form a disulfide bond only if their Cβ-Cβ distance is less than about 5 Å (34), the formation of the engineered disulfides provided us with a sensitive indicator for local conformational variability. When UvrA-Trunc was titrated in the CuPh oxidation reactions without nucleotide, we consistently observed dose-dependent cross-linking in TRCF-D2:RID (Fig. S3C), suggesting that UvrA-Trunc binding promotes a relative conformation of D2 and RID that favors cross-linking, similar to ATPγS binding. This is also consistent with a modestly larger apparent Stokes radius of oxidized TRCF-D2:RID suggested by gel filtration analysis (Fig. S5). As with ATPγS, we observed the opposite trend in TRCF-D2:D7 (Fig. 4D), suggesting that, upon UvrA binding, D7 adopts a conformation incompatible with formation of the D2–D7 cross-link. When higher CuPh concentrations are used with TRCF-A167C, we also observed formation of an intramolecular cross-link of different electrophoretic mobility (Fig. S7B). This disulfide likely forms between C167 and one of the seven cysteines in wild-type TRCF. We can exclude disulfide formation between D2 and D7, as no cysteines are present in D7 (Fig. S1E). Formation of this cross-link was also nucleotide and UvrA-Trunc dependent (Fig. S7B). This suggests that the UvrB homology module may also move during the functional cycle, in agreement with our observation of the closure of the central cavity in ATP-bound TRCF (Fig. 3B).

To test if TRCF release of stalled TECs also involves a repositioning of D7 to fully activate TRCF and promote efficient binding of UvrA, we compared dissociation of TECs stalled by nucleotide deprivation by TRCF and TRCF-D2:D7. Like wild type, TRCF-D2:D7 displaced the TEC in both the reduced and the cross-linked states (Fig. 4B). In ATPase assays (Fig. 4A), we observed a reduction in the ATPase rates for both Cys mutants, but the effect was the largest for oxidized TRCF-D2:D7 even though our preparation contained a small amount (~10%) of non-cross-linked TRCF-D2:D7 species (Fig. S7A). Thus, we can conclude that the oxidized species is greatly impaired in ATPase activity in the absence of RNAP. Fluorescence anisotropy experiments (Fig.S2 B–D) indicate that the affinity of reduced TRCF-D2:D7 for DNA is similar to wild type (K_d of 131 ± 17 nM compared with 118 ± 11 nM), whereas in oxidized TRCF-D2:D7 it is greatly reduced (K_d of 1798 ± 300 nM). This suggests that, by tethering D2 to D7, the naked DNA-binding and DNA translocation activities (in the presence of RNAP) can be uncoupled. The ability of oxidized, ATPase-deficient TRCF-D2:D7 to displace stalled TECs (Fig. 4B) implies that the ATPase function is stimulated by binding to TECs. Indeed, TECs stimulated ATP hydrolysis threefold compared with naked DNA template (Fig. 4E). Furthermore, TEC dramatically increased ATP turnover by oxidized TRCF-D2:D7, restoring it to about 30% of the total P_i released by wild type, correlating well with the more modest reduction in the RNA release by this variant. A stoichiometric titration of dsDNA in oxidation reactions revealed that naked DNA substrate does not alter the propensity to cross-link (Fig. S7C) and, consequently, the dynamic equilibrium of TRCF conformations. Thus, the robust TEC release activity of oxidized TRCF-D2:D7, which is greatly impaired in DNA binding, suggests that the initial recognition of a stalled TEC is likely provided through specific protein–protein contacts between the RID and the β-subunit of RNAP (5, 18, 35) and that protein–DNA contacts play a secondary role.

Discussion

Since the discovery of TRCF (36), the mechanistic details of UvrA recruitment, including the mode and timing of UvrA binding, have remained unknown. Here, we show how the binding of UvrA to TRCF occurs at the interface of domains D2 and D7 and closely mimics contacts between UvrA and UvrB, with residues critical for the interaction being conserved across and between the TRCF and UvrB families (Figs. 1–2). Together with functional studies of mutants in which the D2–D7 or the RID-D7 domains were locked by disulfide linkages, our study also establishes that, for UvrA to bind, the C-terminal domain D7 of TRCF has to move relative to its position in apo TRCF. SAXS analysis of the ATPase-deficient mutant TRCF-E730Q revealed that ATP binding leads to repositioning of multiple domains, including the inhibitory D7 (Fig. 3). A disulfide bond engineered across the D2–D7 interface uncouples the DNA-binding and ATPase activity of TRCF in the absence of TECs from translocation on dsDNA, RNA release, and TEC-

stimulated ATP turnover (Fig. 4), suggesting that disruption of the D2–D7 interface (needed for UvrA recruitment) is not required for RNAP release. Our data allow us to take a fresh look at mechanistic models for TCR with a focus on UvrA recruitment.

TRCF Exists in a Dynamic Equilibrium of Conformations. Our data suggest that TRCF exists in a dynamic equilibrium between two (or more) conformational states, a closed repressed conformation, and a more open state that can bind UvrA. The closed conformation predominates in solution in the absence of nucleotide and is characterized by an evolutionarily conserved D2–D7 interaction. This interaction was also observed crystallographically (18), but due to crystal contacts, its physiological relevance remained unclear. Weakening of this interaction did not abolish strand-specific repair in vitro or in vivo (21), but the effects of a tighter D2–D7 interaction on TCR were not explored.

We show that formation of the open state of TRCF is favored upon ATP binding, which results in movement of D7. UvrA binding likely also shifts the equilibrium toward the open conformation, consistent with UvrA inhibiting formation of the D2–D7 and TRCF-A167C cross-links and favoring formation of the D7-RID disulfide (Fig. 4D and Figs. S3C and S7B). However, detection of UvrA binding to full-length TRCF even in the absence of nucleotides (9) indicates that the open state is populated even in the apo protein. In addition to a breathing motion of D7, ATP also induces a repositioning of the D1–D3 module, which likely moves as a rigid body because the crystal structure of D1–D3 in isolation was shown to be identical to that in the context of the full-length protein (22). Recent work identified a protease-sensitive site in the D3-RID linker that is exacerbated in a derepressed TRCF variant, consistent with a rigid-body movement around a hinge located in this linker. The same study also revealed other protease-sensitive sites in the interdomain linkers, corroborating our conclusion that ATP (and likely also TEC) binding results in reorganization of interdomain contacts. The ATP-triggered shift toward an "open" state of TRCF could be interpreted as triggering UvrA recruitment for TCR to occur. However, with ATP, we observe on average only a partial exposure of the UvrA-binding site using SAXS, and, in pull-down assays with TRCF-E730Q (and ATP) under conditions in which we could robustly pull-down UvrA-Trunc, we could detect the TRCF–E739Q/UvrA–Trunc complex only weakly (Fig. S1A), suggesting that ATP alone is not sufficient for complete accessibility to the UvrA-binding surface. Furthermore, increased levels of UvrA are inhibitory to TCR (3), arguing that TRCF–UvrA complexes formed before TEC engagement/release may be mechanistically nonproductive.

Autoinhibition of UvrA Binding Is Likely Relieved upon Engaging the DNA Damage. Despite previous attempts, failure to detect pathway intermediates such as TEC-TRCF-UvrAB or DNA-TRCF-UvrAB (3, 9) has left mechanistic details of the coupling largely unknown. Models for TCR differ in the timing of UvrA recruitment, occurring upon completion of RNAP release (4, 18) (mechanism I, Fig. 5) or upon engaging the RNAP (4, 18, 22) (mechanism II, Fig. 5).

In both mechanisms, the stalled TEC has a critical role. It acts as a DNA damage sensor, activates the dsDNA translocase activity of TRCF (32), and, as our data indicate (Fig. 4E), stimulates ATP turnover. Thus, TRCF appears to function akin to eukaryotic dsDNA translocases, such as chromatin-remodeling factors, which are often stimulated preferentially by nucleosome substrates over naked DNA (37).

ATPase hyperactivity can be achieved even in the absence of RNAP by substitutions weakening D2–D7 (21) or D1–D6 contacts (38, 39). Truncations lacking D7 or D1–D3, unlike full-length protein, can translocate on naked DNA (22, 32) These observations are consistent with both mechanisms in Fig. 5, in which disruption of the D2–D7 contacts enables activation in the absence of RNAP. Consequently, locking the D2–D7 interface is expected to prevent this activation, in agreement with our observation that cross-linking D2 to D7 significantly affects ATP turnover in the absence of RNAP (Fig. 4A). However, the interdomain cross-link does not abolish RNAP release (Fig. 4B), arguing that motions of
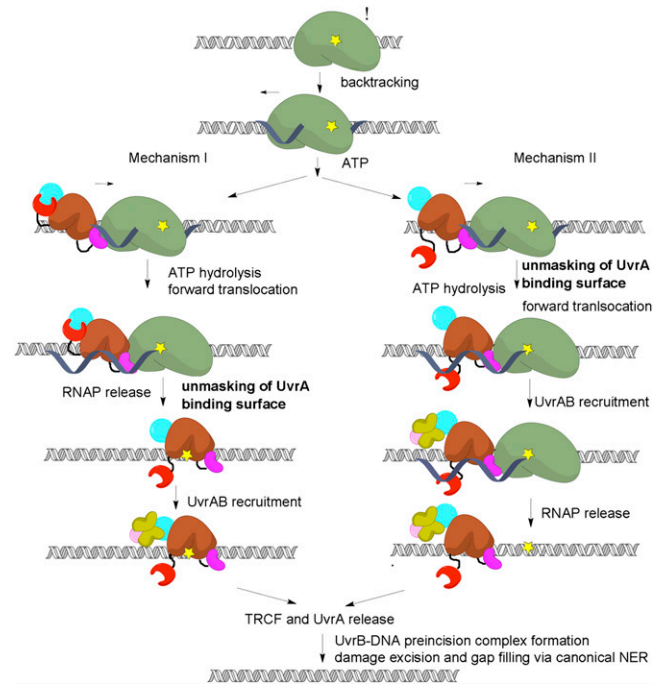

Fig. 5. TCR mechanisms. RNAP (green) stalls at DNA lesions (yellow) in the template strand and backtracks, recruiting TRCF, which promotes forward translocation of RNAP using ATP hydrolysis by the translocase module (brown) and, eventually, TEC dissociation. Next, the UvrAB complex is recruited by virtue of the unmasking of the UvrA-binding surface in D2 by motion of D7. The timing of UvrA recruitment differs in these two models, but our data argue for a sequential model (mechanism I). The pathway continues with formation of an UvrB–DNA preincision complex, subsequent DNA incisions, and gap filling (36).

D7 are not essential for TEC displacement and that the ATPase (in the absence of TEC) and the ATP-dependent translocase functions appear to be regulated differently. This agrees with recent in vivo and in vitro studies showing that triple substitutions at the D2–D7 interface result in different functional defects. D2 mutations abolish dsDNA translocation but do not compromise RNAP release, whereas substitutions in D7 affect neither dsDNA translocation nor RNAP release (21). The nature of the translocase activation in the presence of RNAP remains unknown, but our results argue against the requirement for a complete disruption of the D2–D7 contacts.

Although D7 repositioning must occur for productive UvrAB recruitment, the latter is required only at a site of damage. RNAP may stall for various reasons, and unmasking the UvrA-binding surface in the absence of RNAP-stalling lesions may have detrimental effects on cell viability. Indeed, cells expressing truncations lacking D7 are more sensitive to UV radiation, and despite efficient RNAP displacement activity in vitro (32), repair DNA less efficiently in vivo and in vitro, perhaps due to diverting rate-limiting UvrA from NER (9, 21).

What triggers productive UvrA recruitment? Among possible scenarios are the following: (i) loading/translocation on the DNA, (ii) interactions with the TEC, and (iii) binding to or near the DNA lesion coupled to/following RNAP displacement. D2–D7 interface disruption is not required for RNA release (Fig. 4) and, consequently, not required for loading/translocation on DNA. Importantly, the inhibitory effect of excess UvrA on TCR can be relieved by supplementation with TRCF (3), suggesting that UvrA-bound TRCF may be incompetent for one of the steps required for coupling, e.g., RNAP/DNA binding and/or translocation. Taken together, these observations favor the last scenario (mechanism I in Fig. 5). In this model, a fully productive complex forms only upon TRCF binding to or close to the exposed DNA lesion, which triggers complete unmasking of the UvrA interface. To

CELL BIOLOGY

gain access to the lesion, TRCF must first remove RNAP from it. This occurs through forward translocation (5, 8) during which RNAP "slides off" and releases the nascent RNA; however, it is not known whether the template DNA is released simultaneously. Following RNA release, TRCF and RNAP may maintain their interactions with each other and the DNA, allowing TRCF to slide toward the lesion. In this model, it is the recognition of the lesion (likely through local distortions in the DNA) that triggers UvrA recruitment. Once TRCF binds to UvrAB and promotes UvrB dissociation from UvrA (9), and possibly its loading onto DNA (40), TRCF likely dissociates from the DNA together with UvrA to leave behind a tight UvrB–DNA complex required for all subsequent incision events.

With TRCF engaged at the lesion, one would expect that global NER and TCR may differ in their requirements for nondamaged/damaged DNA discrimination by UvrA. The presence of TRCF does not render any of the subunits of the Uvr system redundant. Indeed, UvrA is required for UvrB loading, and UvrB residues that are important for DNA damage recognition and local strand separation are equally important for global NER and TCR (21). However, it has been shown that TCR exhibits a less stringent requirement for damage recognition by UvrA (21), likely because the lesion is recognized initially by RNAP, and perhaps later by TRCF. Together with our observation that D2–D7 cross-linking has a larger effect on UvrA binding than RNA release, these considerations also support mechanism I, which proceeds through an UvrAB-TRCF-DNA damage intermediate rather than through the TEC–TRCF–UvrAB complex of mechanism II. Further studies will be necessary to elucidate the precise sequence of events occurring during TCR, especially early on, during recruitment of NER machinery, damage detection, and preincision complex formation.

In a broader context, the D7-mediated occlusion of the D2 UvrA-binding interface that we observed may be essential for the TCR-independent functions of TRCF. In the case of head-on collisions of RNAP with replication forks (11), as well as transcriptional termination (17) and carbon catabolite repression (16), only the RNAP displacement activity of TRCF is essential, whereas the NER recruitment function is at least dispensable, if not detrimental. Our analysis thus brings insight into a general mechanism for UvrA-binding inhibition in TRCFs and suggests that TRCF function relies on a fine temporal and context-dependent tuning of its various activities.

Materials and Methods

A full description of the materials and methods used can be found in *SI Materials and Methods*.

X-Ray Crystallography. Crystals of TRCF-Trunc/UvrA-Trunc were obtained via vapor diffusion and were pronouncedly anisotropic. The best diffracting crystals were obtained in 10% PEG 3350 and 4% tacsimate (pH 4.8). Cryoprotection was achieved with 14% PEG 3350, 4% tacsimate (pH 4.8), 20% ethylene glycol and by plunging the crystals in liquid nitrogen. Data were collected remotely at beamline 8.2.1 at the Advanced Light Source (ALS) at 1 Å wavelength and 100 K. Further details are included in *SI Materials and Methods*.

SAXS Analysis. Data were collected at the Sibyls synchrotron beamline (ALS) at concentrations of 1–7 mg/mL protein for TRCF-E730Q and 0.3–2 mg/mL protein for TRCFΔ(D1-D3)E730Q, respectively, in triplicate or more at 10 °C. Further details are presented in *SI Materials and Methods*.

1. Hanawalt PC, Spivak G (2008) Transcription-coupled DNA repair: Two decades of progress and surprises. *Nat Rev Mol Cell Biol* 9:958–970.
2. Selby CP, Sancar A (1990) Transcription preferentially inhibits nucleotide excision repair of the template DNA strand in vitro. *J Biol Chem* 265:21330–21336.
3. Selby CP, Sancar A (1995) Structure and function of transcription-repair coupling factor. II. Catalytic properties. *J Biol Chem* 270:4890–4895.
4. Selby CP, Sancar A (1993) Molecular mechanism of transcription-repair coupling. *Science* 260:53–58.
5. Park J-S, Marr MT, Roberts JW (2002) *E. coli* transcription repair coupling factor (Mfd protein) rescues arrested complexes by promoting forward translocation. *Cell* 109:757–767.
6. Deaconescu AM, Savery N, Darst SA (2007) The bacterial transcription repair coupling factor. *Curr Opin Struct Biol* 17:96–102.
7. Roberts J, Park JS (2004) Mfd, the bacterial transcription repair coupling factor: Translocation, repair and termination. *Curr Opin Microbiol* 7:120–125.
8. Park JS, Roberts JW (2006) Role of DNA bubble rewinding in enzymatic transcription termination. *Proc Natl Acad Sci USA* 103:4870–4875.
9. Selby CP, Sancar A (1995) Structure and function of transcription-repair coupling factor. I. Structural domains and binding properties. *J Biol Chem* 270:4882–4889.
10. Selby CP, Sancar A (1990) Structure and function of the (A)BC excinuclease of Escherichia coli. *Mutat Res* 236:203–211.
11. Pomerantz RT, O'Donnell M (2010) Direct restart of a replication fork stalled by a head-on RNA polymerase. *Science* 327:590–592.
12. Han J, Sahin O, Barton YW, Zhang Q (2008) Key role of Mfd in the development of fluoroquinolone resistance in Campylobacter jejuni. *PLoS Pathog* 4:e1000083.
13. Lee GH, et al. (2009) The Helicobacter pylori Mfd protein is important for antibiotic resistance and DNA repair. *Diagn Microbiol Infect Dis* 65:454–456.
14. Ayora S, Rojo F, Ogasawara N, Nakai S, Alonso JC (1996) The Mfd protein of Bacillus subtilis 168 is involved in both transcription-coupled DNA repair and DNA recombination. *J Mol Biol* 256:301–318.
15. Dutta D, Shatalin K, Epshtein V, Gottesman ME, Nudler E (2011) Linking RNA polymerase backtracking to genome instability in E. coli. *Cell* 146:533–543.
16. Zalieckas JM, Wray LVJ, Jr., Ferson AE, Fisher SH (1998) Transcription-repair coupling factor is involved in carbon catabolite repression of the *Bacillus subtilis* hut and gnt operons. *Mol Microbiol* 27:1031–1038.
17. Washburn RS, Wang Y, Gottesman ME (2003) Role of E.coli transcription-repair coupling factor Mfd in Nun-mediated transcription termination. *J Mol Biol* 329:655–662.
18. Deaconescu AM, et al. (2006) Structural basis for bacterial transcription-coupled DNA repair. *Cell* 124:507–520.
19. Assenmacher N, Wenig K, Lammens A, Hopfner KP (2006) Structural basis for transcription-coupled repair: The N terminus of Mfd resembles UvrB with degenerate ATPase motifs. *J Mol Biol* 355:675–683.
20. Pakotiprapha D, Liu Y, Verdine GL, Jeruzalmi D (2009) A structural model for the damage-sensing complex in bacterial nucleotide excision repair. *J Biol Chem* 284:12837–12844.
21. Manelyte L, Kim YI, Smith AJ, Smith RM, Savery NJ (2010) Regulation and rate enhancement during transcription-coupled DNA repair. *Mol Cell* 40:714–724.
22. Murphy MN, et al. (2009) An N-terminal clamp restrains the motor domains of the bacterial transcription-repair coupling factor Mfd. *Nucleic Acids Res* 37:6042–6053.
23. Selby CP, Sancar A (1993) Transcription-repair coupling and mutation frequency decline. *J Bacteriol* 175:7509–7514.
24. Srivastava DB, Darst SA (2011) Derepression of bacterial transcription-repair coupling factor is associated with a profound conformational change. *J Mol Biol* 406:275–284.
25. Pakotiprapha D, et al. (2008) Crystal structure of Bacillus stearothermophilus UvrA provides insight into ATP-modulated dimerization, UvrB interaction, and DNA binding. *Mol Cell* 29:122–133.
26. Deaconescu AM, Darst SA (2005) Crystallization and preliminary structure determination of Escherichia coli Mfd, the transcription-repair coupling factor. *Acta Crystallogr Sect F Struct Biol Cryst Commun* 61:1062–1064.
27. Truglio JJ, et al. (2004) Interactions between UvrA and UvrB: The role of UvrB's domain 2 in nucleotide excision repair. *EMBO J* 23:2498–2509.
28. Svergun DI (1999) Restoring low resolution structure of biological macromolecules from solution scattering using simulated annealing. *Biophys J* 76:2879–2886.
29. Volkov V, Svergun DI (2003) Uniqueness of ab initio shape determination in small-angle scattering. *Biophys J* 80:2946–2953.
30. Prabha S, Rao DN, Nagaraja V (2011) Distinct properties of hexameric but functionally conserved Mycobacterium tuberculosis transcription-repair coupling factor. *PLoS ONE* 6:e19131.
31. Dürr H, Flaus A, Owen-Hughes T, Hopfner KP (2006) Snf2 family ATPases and DExx box helicases: Differences and unifying concepts from high-resolution crystal structures. *Nucleic Acids Res* 34:4160–4167.
32. Smith AJ, Szczelkun MD, Savery NJ (2007) Controlling the motor activity of a transcription-repair coupling factor: Autoinhibition and the role of RNA polymerase. *Nucleic Acids Res* 35:1802–1811.
33. Reyes N, Ginter C, Boudker O (2009) Transport mechanism of a bacterial homologue of glutamate transporters. *Nature* 462:880–885.
34. Careaga CL, Falke JJ (1992) Thermal motions of surface alpha-helices in the D-galactose chemosensory receptor. Detection by disulfide trapping. *J Mol Biol* 226:1219–1235.
35. Westblade LF, et al. (2010) Structural basis for the bacterial transcription-repair coupling factor/RNA polymerase interaction. *Nucleic Acids Res* 38:8357–8369.
36. Selby CP, Witkin EM, Sancar A (1991) Escherichia coli mfd mutant deficient in "mutation frequency decline" lacks strand-specific repair: In vitro complementation with purified coupling factor. *Proc Natl Acad Sci USA* 88:11574–11578.
37. Hauk G, Bowman GD (2011) Structural insights into regulation and action of SWI2/SNF2 ATPases. *Curr Opin Struct Biol* 21:719–727.
38. Hunnewell ME (2008) Probing the conformational changes in the repair enzyme Mfd using mutant protein constructs, MS thesis (University of Massachusetts, Amherst, MA).
39. Hsieh C-H (2010) Probing the activation mechanism of transcription-coupled repair factor Mfd, MS thesis (University of Massachusetts, Amherst, MA).
40. Theis K, et al. (2000) The nucleotide excision repair protein UvrB, a helicase-like enzyme with a catch. *Mutat Res* 460:277–300.

Supporting Information

Deaconescu et al. 10.1073/pnas.1115105109

SI Materials and Methods

Molecular Biology, Protein Expression, and Purification. Transcription-repair coupling factor, TRCF-E730Q and all Cys point mutants (TRCF-A167C, TRCF-H527C, TRCF-A1051C, and TRCF-A1031C) were constructed in the pAD6 plasmid encoding wild-type TRCF by site-directed mutagenesis using the Quikchange kit (Agilent). They were overexpressed and purified as described before (1); where appropriate, gel filtration chromatography was performed immediately before SAXS data collection. Samples were then concentrated and dialyzed against a buffer containing 150 mM NaCl, 20 mM Tris (pH 8.0), 10 mM MgCl$_2$, and 5 mM DTT with and without 5 mM ADP/ATP, respectively. Gel filtration in the absence/presence of nucleotides was performed on a Superdex200 10/300 column (GE Healthcare) by injecting 200 µg TRCF-E730Q and 1 mg TRCFΔ(D1-D3)E730Q and by using buffer conditions identical to those used for SAXS sample preparation. The pAD61 construct encoding TRCFΔ(D1-D3)E730Q (residues 479–1,148 in TRCF) used for SAXS measurements was purified as wild-type TRCF.

The H527C A1031C and A167C G1051C double mutants were created in two Quikchange mutagenesis steps using pAD6 as a template to yield pAD54 and pAD79, respectively, and purified as wild type. No reducing agent was added to buffers used in the purification of TRCF Cys single or double mutants.

For crystallography, the TRCF and UvrA truncations (TRCF-Trunc and UvrA-Trunc, respectively) were generated as follows. Sequences were amplified via PCR using pAD6 and pUNC45 (2) as templates and cloned between the NheI/HindIII sites of a pET28-a derivative to generate pAD36 (encoding residues 127–213 of *Escherichia coli* TRCF) and pAD42 (encoding residues 131–250 of *E. coli* UvrA), respectively. Cultures of transformed Rosetta2 (DE3)pLysS cells were grown to an OD of 0.6 and induced with 1 mM isopropyl-β-D-thiogalactoside at 30 °C for 3 h. For purification, pellets were resuspended in 0.5 M NaCl, 20 mM Tris (pH 8), 5% glycerol, and 2 mM β-mercaptoethanol and purified using Ni^{2+} chromatography as described in (3). After overnight cleavage of the His-tag with Prescission protease, a second subtractive immobilized metal-affinity chromatography step was used to remove the remaining uncleaved recombinant protein. A final gel filtration step on a Sephacryl S-100 column was performed in 100 mM NaCl, 20 mM Tris (pH 8), and 10 mM DTT. For complex assembly, equimolar quantities of TRCF-Trunc and UvrA-Trunc were mixed and incubated on ice.

Pull-Down Assays. For pull-down assays, TRCF derivatives were immobilized to magnetic metal-chelating Dynabeads (Invitrogen) via an N-terminal hexahistidine tag cleavable with Prescission protease (GE Healthcare). Briefly, 250 pmol of purified TRCF-E730Q or TRCF-Trunc were mixed with purified UvrA-Trunc in a 1:4 stoichiometric ratio and incubated for 30 min at room temperature in binding buffer [100 mM NaCl, 20 mM Tris (pH 7.5), 5% glycerol]. Protein sample was then added to equilibrated Dynabeads and incubated for 30 min at 4 °C. Beads were then washed with binding buffer and resuspended in binding buffer supplemented with Prescission protease (GE Healthcare) and 5 mM DTT and further incubated overnight at 4 °C. Beads were then collected on the side of tubes via a magnet, and samples were withdrawn and subjected to SDS/PAGE on 4–12% gels followed by staining with Coomassie Blue.

ATP Binding and ATPase Assays. ATP binding was assayed using photo-cross-linking of radiolabeled ATP to protein. Four micrograms of purified protein was incubated with 10 µM ATP spiked with 5 µCi α-[^{32}P]ATP (3,000 mCi/mmol; Perkin-Elmer) in 150 mM NaCl, 20 mM Tris (pH 8), 1 mM DTT, and 5% glycerol in a reaction volume of 20 µL without/with the indicated amount of competitor ATP for 15 min at 20 °C. Samples were then placed as small drops on cooled parafilm-wrapped microscope slides on ice and irradiated at 254 nm in a Stratalinker 1800 UV source for 2 min (0.24 J/cm^2). Samples were then mixed with SDS loading buffer, boiled, and run on 4–16% Bis-Tris SDS/PAGE (Invitrogen). Gels were stained for protein with Coomassie Blue and exposed using a phosphor storage screen.

ATPase assays were carried out in triplicate at 25 °C using the EnzCheck Phosphate Assay kit (Molecular Probes) with a buffer consisting of 100 mM NaCl, 50 mM Hepes (pH 7.4), 10 mM MgCl$_2$, 5% glycerol, and 5 mM ATP at protein concentrations ranging from 0.5 to 4 µM. Turnover numbers were obtained by fitting the linear portion of the curves using regression analysis and calculating the slope of the linear fit with the kinetics module of Swift II software (Biochrome).

Stimulated ATPase Assays. For testing the effects of ternary elongation complexes (TECs) on ATP turnover by TRCF, stalled TECs were prepared by nucleotide starvation as for RNA polymerase (RNAP) release assays. Briefly, 600 nM TECs (or naked ~150-bp dsDNA template) was mixed with 0.25 mM cold ATP spiked with 10 µCi of γ-[^{32}P]ATP, followed by addition of 800 nM TRCF at time 0. Reactions were then incubated at 37 °C for 2, 5, and 10 min and quenched by addition of an equal volume (2 µL) of acetic acid. A total of 0.4 µL of the mixture was analyzed by thin layer chromatography on polyethylenimine cellulose plates (Sigma), which were developed in 750 mM KH$_2$PO$_4$ (pH 3.5). Released ^{32}P$_i$ was visualized and quantified by phosphorimaging. The reported percentage of Pi released was calculated according to the following relationship:

$$\% \text{ of } P_i = P_i \text{ intensity} * 100/\text{total signal in the relevant lane}$$
$$(\text{corresponding to both hot ATP and hot } P_i).$$

Design and Biochemical Studies of Disulfide-Locked Mutants. For rational design of disulfide bonds that would restrain D7, we have used Disulfide by Design (4), a software package that, given a protein structure coordinate file [e.g., Protein Data Bank (PDB) ID 2EYQ], computes all possible proximal residue pairs with a geometry consistent with the geometry of a disulfide bond. This allowed us to identify H527 and A1031 as good candidate substitutions. However, this in silico tool did not predict any suitable residue pair that would tether D2 to D7 (and would prevent exposure of the UvrA-binding surface). We have thus proceeded to design the TRCF-D2:D7 mutant strictly on the basis of spatial proximity considerations by inspection of the crystal structure of nucleotide-free TRCF. We underscore that, in both TRCF-D2:RID and TRCF-D2:D7, some movements of the cross-linked domains may still be accommodated.

For cross-linking studies, protein was first reduced by incubation with 20 mM tris(2-carboxyethyl)phosphine on ice for 1 h, and buffer was subsequently exchanged to 0.1 M NaCl, 50 mM Hepes (pH 7.0), and 10 mM MgCl$_2$ with/without 5 mM ADP or ATPγS. Oxidative disulfide cross-linking reactions were carried out in the presence of a phenanthroline (CuPh) catalyst at the indicated concentrations for 10 min at room temperature and quenched with 50 mM iodoacetamide and SDS loading buffer supplemented with 50 mM EDTA in order to chelate the cupric

ions. SDS/PAGE page was carried out on 3–8% Tris-acetate gels (Invitrogen) under standard nonreducing or reducing conditions.

For cross-linking studies in the presence of UvrA-Trunc, a CuPh concentration of 4 μM was used with 4 μg of TRCF mutant and increasing concentrations of purified UvrA-Trunc in a buffer consisting of 100 mM NaCl, 20 mM Tris (pH 7.5), 10 mM MgCl$_2$, and 5% glycerol. The TRCF-D2:D7:UvrA-Trunc stoichiometry of the reactions shown in Fig. 2 were 2:1, 1:3, 1:5, and 1:10. Reactions were carried out for 10 min at room temperature and were terminated and analyzed as above. Densitometry was carried out using the Kodak-1D software. We note the weak staining of UvrA-Trunc, which is much smaller than full-length TRCF (~13 versus 130 kDa). Under the electrophoresis conditions required for optimum separation of reduced from oxidized species, UvrA-Trunc migration overlaps with the dye front, making its visualization more difficult as in Fig. 4D. Under a shorter electrophoresis run time, UvrA-Trunc can be clearly visualized (Fig. 4D, lane 10). For CuPh-catalyzed oxidation of TRCF-D2:RID (Fig. S3C), uncleaved UvrA-Trunc carrying an N-terminal hexahistidine tag was used.

For cross-linking of TRCF variants in the presence of dsDNA, we have used the same 90-bp dsDNA fragment and buffer system used in our fluorescence anisotropy assays. Protein and DNA were mixed in the stoichiometric ratios indicated in Fig. S7C (from 4:1–1:3 of TRCF variant:DNA). Oxidation was initiated by addition of 10 μM CuPh (for TRCF-D2:D7) and 4 μM CuPh (for TRCF-D2:RID) and stopped as described above, and samples were subjected to nonreducing SDS/PAGE on 3–8% Tris-acetate gels. DNA integrity was also assessed using 5% agarose electrophoresis and ethidium bromide staining. White shadow immediately above the DNA bands in Fig. S7D is due to the tracking dye. Cuprous ions and phenanthroline are known to form a chemical nuclease (5) that can fragment the DNA present in the oxidation reactions. In the presence of reducing agent, cupric ions and phenanthroline could potentially be converted to chemical nuclease, degrading the DNA and confounding the assays. Although no reducing agent was added in the buffer used for these oxidation reactions, carryover of reducing agent from the previous experimental step (the complete reduction of the Cys variants and buffer exchange) represents a concern. However, agarose electrophoresis indicates that DNA is not affected under experimental conditions.

Size-exclusion chromatography of TRCF-D2:RID/TRCF-D2:D7 and TRCF was carried out on a Superdex 200 10/300 gel filtration column (GE Healthcare) run in a buffer consisting of 0.25 M NaCl, 20 mM Tris (pH 8), 5% glycerol, and no reducing agent. For calibration purposes, a gel filtration calibrant kit (Bio-Rad) was used in conjunction with purified catalase from *Aspergillus niger* (Sigma Aldrich), which provides a standard of a molecular weight (250 kDa) similar to the theoretical molecular weight of a putative TRCF dimer (260 kDa).

Fluorescence Anisotropy Assays. A double-stranded 90-bp DNA fragment was generated by conventional PCR amplification with flanking primers, one of which contains a HEX fluorophore at the 5′ end, and the product was further purified using conventional agarose gel purification methods. Fluorescently labeled DNA (20 nM) was titrated with increasing concentrations of wild-type TRCF or TRCF-E730Q. DNA was added into 1.5 mL of buffer containing 20 mM Hepes (pH 7.5), 50 mM NaCl, and 2 mM β-mercaptoethanol, with or without 2 mM ATPγS (Merck), as indicated. To assess binding by TRCF-D2:D7, titrations were performed with oxidized protein in 20 mM Hepes (pH 7.5), 50 mM NaCl, and 2 mM ATPγS without DTT. Reduced TRCF-D2:D7 was also assayed under a similar buffer system, which included 4 mM DTT. After the addition of TRCF variants, the reaction was equilibrated for 5 min at 25 °C before measurements were recorded. Fluorescence anisotropy was measured at

555 nm using a F-7000 fluorescence spectrophotometer (Hitachi). The K_d values were calculated from three independent experiments using the Micromath Scientist software package.

DNaseI Footprinting Assays. Footprinting assays used a template containing the T7A1 promoter and a 147-nt G-less initial transcribed region, which was generated by PCR amplification using the pRL596 plasmid. The nontemplate DNA strand primer was end-labeled with [P^{32}]-γATP (Perkin-Elmer) using polynucleotide kinase from Epicentre and purified using G-50 spin columns (GE Healthcare). PCR products were gel-purified using a gel purification kit (Promega). The halted C147 TECs were assembled at 37 °C for 20 min with 20 nM of labeled DNA fragment; 400 nM wild-type holo *E. coli* RNAP; 25 μM ATP, GTP, and CTP; and 100 μM ApU in transcription buffer (44 mM Tris·HCl, 14 mM MgCl$_2$, 20 mM NaCl, 5% glycerol, 0.1 mM EDTA, pH 7.9). Then ATPγS was added to 2 mM, and TRCF variants were added to 120 nM (wild type and TRCF-D2:D7) or 250 nM (TRCF-E730Q). After 2 min of incubation, complexes were treated with 0.15 units of DNaseI (Epicentre) for 1 min, and digestions were then quenched by the addition of an equal volume of phenol. Samples were subjected to phenol-chloroform extraction and precipitated with ethanol. Pellets were then dissolved in 96% formamide, heated at 95 °C for 3 min, and analyzed on 7 M urea, 8% (wt/vol) acrylamide:bisacrylamide (19:1) denaturing gels. To determine footprint boundaries, a dideoxy sequencing ladder using labeled primer was generated with a SequiTherm kit (Epicentre). As controls, digestion reactions were carried out in the absence of added proteins or in the presence of TRCF alone (without RNAP, but with all other components). The boundaries of C^{147} in the absence or in the presence of TRCF were established using trace analysis with the trace obtained in the absence of proteins as a baseline (black in Fig. S2F). In the halted TEC, positions from −14 to +15 (relative to the active site of RNAP) are protected against DNaseI cleavage, consistent with the results obtained under the same conditions with other defined TECs (6). TRCF binds specifically to the TEC, extending the upstream boundary of DNA protection from 14 to 39 bp. All TRCF variants bound efficiently to the halted TEC despite their differences in affinity to naked DNA and the efficiency of RNA release observed in the experiments described above. Under these reaction conditions, no specific DNA protection by TRCF was observed in the absence of RNAP.

RNA Release Assays. RNA release assays were carried out with modifications using a previously published protocol (7), and used a template derived from a previously described plasmid, pIA226 (8), containing the phage λ P$_R$ promoter followed by a C-less transcribed region. This transcription template was prepared by PCR amplification with flanking primers, one of which contained a triethylene-glycol-coupled biotin (TEG-biotin) moiety at its 5′ end. [α^{32}P]-labeled halted A26 TEC was formed by CTP deprivation in TGA10 buffer (20 mM Tris-acetate, 20 mM Na acetate, 10 mM Mg acetate, 1 mM DTT, 0.1 mM EDTA, 5% glycerol, pH 7.9) and immobilized on streptavidin-coated magnetic beads (DynaBeads T1, Invitrogen). Beads were washed three times with 1 mL of the reaction buffer (TGA10 without DTT) containing 200 mM NaCl to remove abortive RNA products and any residual reducing agent and incubated with TRCF (at 40 or 4 nM final concentration) at 37 °C for 1 min. Reactions were initiated by addition of 2 mM ATP, and RNA released into the supernatant was removed at various time points, mixed with an equal volume of 2× STOP solution [10 M urea, 50 mM EDTA, 45 mM Tris-borate (pH 8.3), 0.1% bromophenol blue, 0.1% xylene cyanol], and loaded onto a 10% denaturing urea-acrylamide (19:1) gel in a buffer consisting of 45 mM Tris, 45 mM boric acid, 1 mM EDTA.

The ability of the cross-linked TRCF-D2:D7 variant to dissociate TECs (Fig. 4B) could be explained if the disulfide bond in this variant were reduced under the conditions of the RNA release, e.g., due to the presence of an unidentified reducing agent not removable by washing of the beads. Formation of the disulfide bridge between Cys167 and Cys1051 substantially alters the mobility of TRCF-D2:D7, allowing us to evaluate this possibility directly. We assembled mock reactions on three different types of DynaBeads beads (A–C, where B was the batch used for the RNA release assays) under the conditions similar to those in Fig. 4B, except that (i) the ^{32}P-labeled GTP was omitted and (ii) TRCF-D2:D7^{ox} protein was present at 500 nM to allow for in-gel detection. As a control, TRCF-D2:D7^{ox} alone was treated with DTT at the indicated concentrations. The reactions were incubated at 37 °C for 16 min (the longest incubation time used in the release assays), stopped, and loaded onto a 3–8% Tris-acetate gel, as shown in Fig. S3B. There was no evidence for reduction of the D2–D7 disulfide due to the magnetic beads used.

Limited Proteolysis. Limited proteolysis of TRCF in the absence and presence of the nucleotides ADP and ATPγS/ATP was carried out using trypsin, chymotrypsin, and subtilisin (Sigma-Aldrich). Protein (25 µg) was mixed with decreasing concentrations of protease at 1:1, 1:10, 1:100, and 1:1,000 protease-to-protein molar ratio and incubated at room temperature for 30 min. Reactions were carried out in a buffer consisting of 100 mM NaCl, 20 mM Tris (pH 8.0), and 10 mM MgCl$_2$ (with and without 5 mM ADP and ATPγS, respectively) and stopped by the addition of 10 mM PMSF and SDS-loading buffer. Samples were subsequently analyzed by SDS/PAGE on 4–12% Bis-Tris gels stained with Coomassie Blue.

Structure Solution and Crystallographic Refinement. For determining the structure of the TRCF–Trunc/UvrA–Trunc complex, data were indexed, reduced, and scaled, and phases were obtained using molecular replacement with Phaser (9). To generate a search model, D2 of E. coli TRCF (PDB ID 2EYQ) was superimposed onto the homologous domain of Geobacillus stearothermophilus UvrB in the UvrA–UvrB complex structure (PDB ID 3FPN), and then the resulting hybrid model was edited on the basis of a pairwise sequence alignment. Coordinates were subsequently refined using iterative cycles of manual building in Coot (10) and PHENIX refinement (11) The final model has no residues in the disallowed region of the Ramachandran plot as assessed using MolProbity. A section of the sigmaA $2|F_o| - |F_c|$ map is presented in Fig. S8B.

SAXS Data Collection and Processing. Data were collected using a detector distance of 1,475 mm and a radiation energy of 12 keV. The buffer consisted of 150 mM NaCl, 20 mM Tris (pH 8), 5 mM DTT, 10 mM MgCl$_2$, and nucleotide at 5 mM, if any, for full-length TRCF, and 250 mM NaCl, 20 mM Tris (pH 8), 10 mM MgCl$_2$, 1% glycerol, and 5 mM DTT with/without 2 mM ADP/ATP for the truncated TRCF variant. Samples and matching buffer were exposed for 0.5 and 5 s for full-length TRCF-E730Q and for 1 and 10 s for TRCFΔ(D1-D3)E730Q, respectively. A second 0.5-s/1-s exposure was recorded after the long exposure to assess radiation damage, which was minimal. Raw scattering data were azimuthally averaged and normalized, and buffer scattering was subtracted using the resident software of the Sibyls beamline. Individual scattering curves for a given state that were collected at different concentrations or exposure duration were merged together using PRIMUS (12) to yield a low-noise interference-free composite curve. Guinier plot analysis was used to assess any potential aggregation, which was not present at protein concentrations less than 4 mg/mL. Radii of

gyration were initially computed on the basis of the Guinier plot analysis in PRIMUS (Fig. S8A) using data points satisfying the requirement $qR_g < 1.3$ (where q represents momentum transfer and R_g the radius of gyration) and subsequently using the second moment of the pair distribution function. Pair distribution function [$p(r)$] and maximum intramolecular distance (D_{max}) values were calculated using the indirect Fourier transform as implemented in GNOM. To properly assess D_{max}, $p(r)$ was initially not constrained to be zero at D_{max}. This gave us an initial estimate of D_{max} that was used in subsequent analysis. For the final processing of the data, $p(r)$ was constrained to become zero at D_{max}. Good agreement was found between the radii of gyration calculated from the second moment of $p(r)$ compared with the values derived from the Guinier plot (Fig. S8A) and shown in Table S2.

Modeling of SAXS Data. Ab initio simulations were performed using GASBOR (13) with structure minimization being carried out against the composite, merged scattering curve rather than the pair distribution function $p(r)$. Fifteen independent simulations were performed for each of the nucleotide-free, ADP-, and ATP-bound TRCF datasets. Sets of simulations were carried out at several r_{max} values to ensure the absence of any artifactual boundary effects resulting from using too small a search volume. The mean χ for the resulting models were 1.4 ± 0.2 for nucleotide-free; 1.4 ± 0.1 for ADP-bound; 1.2 ± 0.07 ATP-bound full-length TRCF; 1.1 ± 0.03 for TRCFΔ(D1-D3); 1.4 ± 0.05 for ADP-bound; and 1.5 ± 0.05 for ATP-bound TRCFΔ(D1-D3). Resulting models were then aligned, averaged, and filtered using the DAMAVER and DAMFILT packages (14). The criterion for including the models in the averaging process was normalized spatial discrepancy (NSD) < mean NSD + 2* variation, where NSD is calculated with SUBCOMP (14) during the initial alignment of the models. According to this criterion, one simulation was discarded for nucleotide-free TRCF-E730Q and TRCFΔ(D1-D3)E730Q, and all 15 simulations were used for all of the other protein samples. The average NSD values for our simulations were as follows: 1.41 ± 0.05 (TRCF-E730Q), 1.45 ± 0.03 (ADP-bound TRCF-E730Q), 1.48 ± 0.04 (ATP-bound TRCF-E730Q), 1.37 ± 0.06 [TRCFΔ(D1-D3)E730Q], 1.24 ± 0.03 [ADP-bound TRCFΔ(D1-D3)E730Q], and 1.26 ± 0.04 [ATP-bound TRCFΔ(D1-D3)E730Q].

We also carried out simulations of the nucleotide-free TRCF using the coordinates of the Cα backbone of apo E. coli TRCF (PDB ID 2EYQ) as input in GASBOR. These simulations converged with similar NSD, but with a slightly higher discrepancy against the raw data, suggesting that seeding the search with the crystal structure coordinates may have trapped the simulation in a local minimum. Therefore, in order to avoid bias, we used only the ab initio nucleotide-free model for analysis. The crystallographic TRCF model was docked as a rigid body using the colores module of SITUS (15) to carry out an exhaustive search and then was locally refined in Chimera (16). Our data did not allow us to generate a physically consistent pseudoatomic model for ADP/ATP-bound TRCF through combined rigid-body fitting of individual domains and combined SAXS/molecular dynamics methods, likely due to the large number of moving domains as well as the presence of multiple interlocking structural elements that are believed to move upon nucleotide binding (namely the TRG motif, hook helices, relay helix, and multiple interdomain loops seen in Fig. 1A). We therefore attempted to place the available crystal structure of nucleotide-free TRCF in the SAXS envelope of ATP-bound TRCF using rigid-body fitting with SITUS and Chimera (15, 16). We obtained two distinct fitting solutions resulting in equally poor cross-correlation (Fig. S6C).

1. Deaconescu AM, Darst SA (2005) Crystallization and preliminary structure determination of Escherichia coli Mfd, the transcription-repair coupling factor. *Acta Crystallogr Sect F Struct Biol Cryst Commun* 61:1062–1064.
2. Thomas DC, Levy M, Sancar A (1985) Amplification and purification of UvrA, UvrB, and UvrC proteins of Escherichia coli. *J Biol Chem* 260:9875–9883.
3. Deaconescu AM, et al. (2002) X-ray structure of Saccharomyces cerevisiae homologous mitochondrial matrix factor 1 (Hmf1). *Proteins* 48:431–436.
4. Dombkowski AA (2003) Disulfide by Design: A computational method for the rational design of disulfide bonds in proteins. *Bioinformatics* 19:1852–1853.
5. Sigman DS, Graham DR, D'Aurora V, Stern AM (1979) Oxygen-dependent cleavage of DNA by the 1,10-phenanthroline cuprous complex. Inhibition of Escherichia coli DNA polymerase I. *J Biol Chem* 254:12269–12272.
6. Krummel B, Chamberlin MJ (1992) Structural analysis of ternary complexes of Escherichia coli RNA polymerase. Deoxyribonuclease I footprinting of defined complexes. *J Mol Biol* 225:239–250.
7. Park J-S, Marr MT, Roberts JW (2002) E. coli transcription repair coupling factor (Mfd protein) rescues arrested complexes by promoting forward translocation. *Cell* 109:757–767.
8. Artsimovitch I, Landick R (2000) Pausing by bacterial RNA polymerase is mediated by mechanistically distinct classes of signals. *Proc Natl Acad Sci USA* 97:7090–7095.
9. McCoy AJ, et al. (2007) Phaser crystallographic software. *J Appl Cryst* 40:658–674.
10. Emsley P, Cowtan K (2004) Coot: model-building tools for molecular graphics. *Acta Crystallogr D Biol Crystallogr* 60(Pt 12 Pt 1):2126–2132.
11. Adams PD, et al. (2002) PHENIX: building new software for automated crystallographic structure determination. *Acta Crystallogr D Biol Crystallogr* 58:1948–1954.
12. Konarev PV, Volkov VV, Sokolova AV, Koch MHJ, Svergun DI, Koch HJ (2003) PRIMUS: A Windows PC-based system for small-angle scattering data analysis. *J Appl Cryst* 36:1277–1282.
13. Svergun DI, Petoukhov MV, Koch MH (2001) Determination of domain structure of proteins from X-ray solution scattering. *Biophys J* 80:2946–2953.
14. Volkov V, Svergun DI (2003) Uniqueness of ab initio shape determination in small-angle scattering. *Biophys J* 80:2946–2953.
15. Wriggers W, Birmanns S (2001) Using situs for flexible and rigid-body fitting of multiresolution single-molecule data. *J Struct Biol* 133:193–202.
16. Pettersen EF, et al. (2004) UCSF Chimera: A visualization system for exploratory research and analysis. *J Comput Chem* 25:1605–1612.
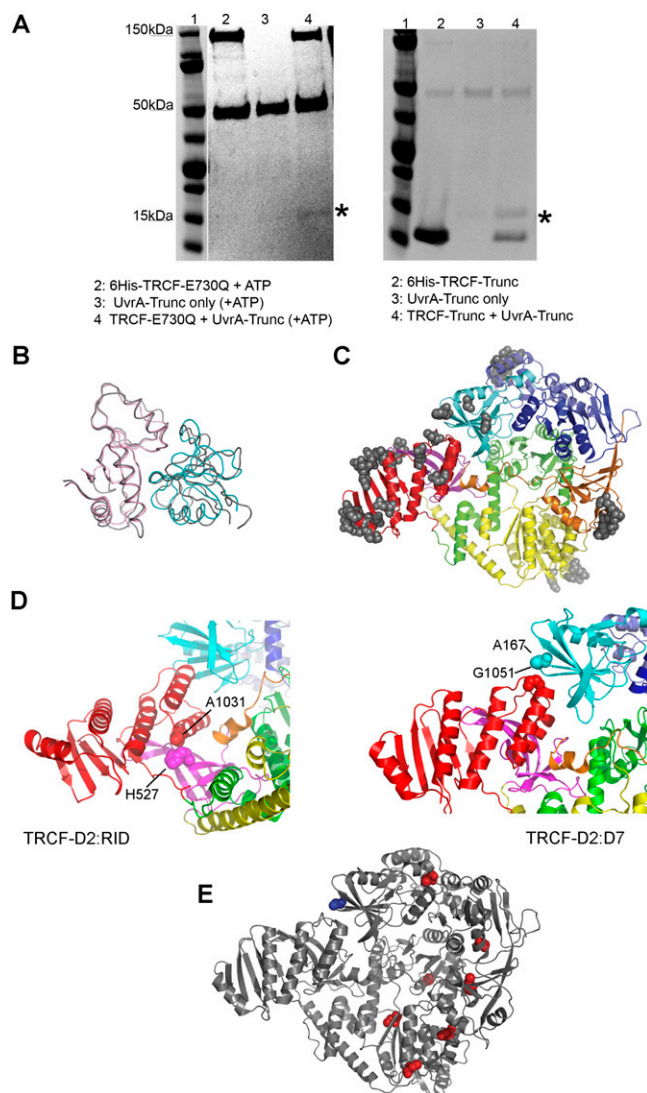
Fig. S1. TRCF and UvrB share a similar mode of binding to UvrA. (*A*) Pull-down assays demonstrating binding of UvrA-Trunc to TRCF derivatives. Complexes were immobilized via a hexahistine tag on TRCF-E730Q (*Left*, in the presence of 5 mM ATPγS) and TRCF-Trunc (*Right*) and then released after washing of the beads via cleavage of the His-tag with Prescission protease. Asterisks indicate bands of pulled-down UvrA-Trunc. Bands migrating near the 50-kDa marker constitute Prescission protease. (*B*) Worm representation of TRCF-Trunc/UvrA-Trunc and the core UvrB/UvrA complex superposed on the Cα atoms of the UvrA domain (root-mean-square displacement of 1.3 Å). TRCF-Trunc is colored in cyan, and UvrA-Trunc and the interacting UvrB domain are shown in pink and gray, respectively. We note in this superposition a small relative rotation of TRCF-Trunc and the UvrB domain relative to the UvrA domain, resulting in a 1.8-Å distance between the centroids of TRCF-Trunc and the UvrB domain. (*C*) TRCF color-coded by domain as in Fig. 1 with residues involved in crystal packing shown as gray spheres. (*D*) Close-up view of domains tethered via disulfide cross-links engineered using Cys substitutions at strategic positions (indicated by spheres) within D2 and RID (TRCF-D2:RID) and D2 and D7 (TRCF-D2:D7). Domains are colored using the coloring scheme of Fig. 1. (*E*) Ribbon representation of TRCF with cysteine residues shown as red spheres and the engineered C167 as blue spheres.
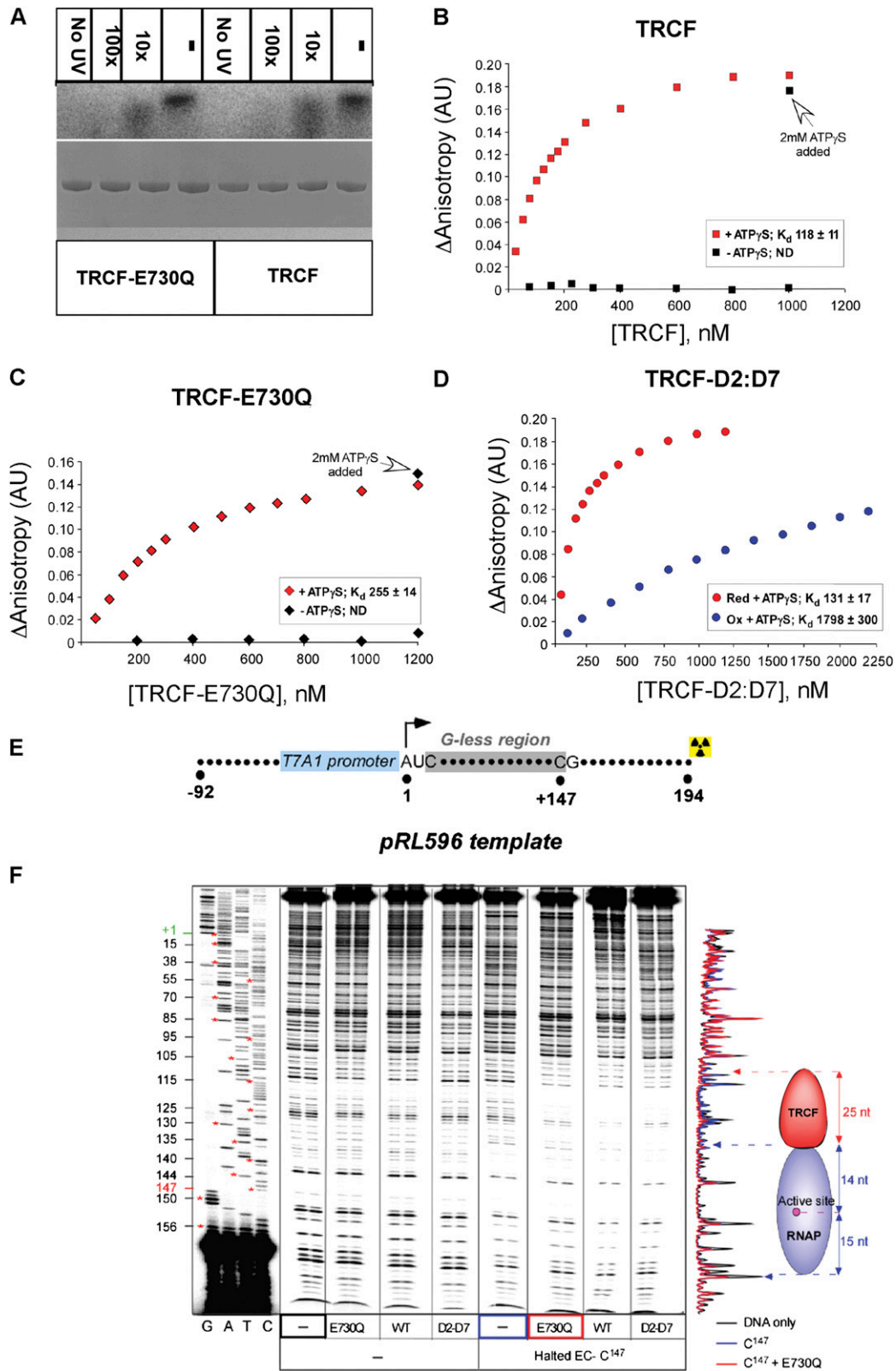
Fig. S2. Biochemical characterization of TRCF variants. (*A*) SDS/PAGE of ATP cross-linked to TRCF and TRCF-E730Q stained with Coomassie Blue (*Lower*) or exposed in a phosphor storage screen (*Upper*). (*B–D*) Representative binding isotherms showing the binding of TRCF variants to a HEX-labeled dsDNA fragment. The units of the determined K_d values are indicated in nanomolar. In control experiments lacking ATP (black symbols), the last sample was measured before and after (as indicated by arrows) the addition of 2 mM ATPγS. Titrations were performed in triplicate with wild-type TRCF (*B*), TRCF-D2:D7 protein both without (blue symbols) or with (red symbols) 4 mM DTT (*D*), as well as the TRCF-E730Q mutant (*C*). (*E*) Schematic representation of the transcription template containing a T7A1 promoter used for generating halted TECs for TRCF binding. Nucleotide positions are indicated in numbers relative to the transcription start site labeled "1." (*F*) Representative denaturing PAGE of the DNaseI digestion reactions (*Right*, loaded in duplicate) as well as the dideoxy sequencing ladder

(*Left*, labeled GATC) used for mapping the binding site of wild-type TRCF, TRCF-E730Q, and oxidized TRCF-D2:D7 (in the D2–D7-labeled lanes) relative to the halted TEC. Numbers on the left of the sequencing ladder mark positions from the transcription start site (corresponding bands are indicated by the asterisks on the gel). As a control, digestion reactions were carried out in the absence of added proteins (the leftmost panel) or in the presence of TRCF alone. The boundaries of C^{147} in the absence (blue) or in the presence of TRCF (red) were established using trace analysis. Digestion of the DNA in the absence of proteins was used as a baseline. In the halted TEC, positions from −14 to +15 [relative to the RNA polymerase (RNAP) active site] are protected against DNaseI cleavage, consistent with results obtained under the same conditions with other defined TECs (6). TRCF binds specifically to the TEC, extending the upstream boundary of DNA protection from 14 to 39 bp. TRCF variants bound efficiently to the halted TEC despite their differences in affinity to the naked DNA and the efficiency of RNA release observed in the experiments described here. Under these reaction conditions, no specific DNA protection by TRCF was observed in the absence of RNAP.
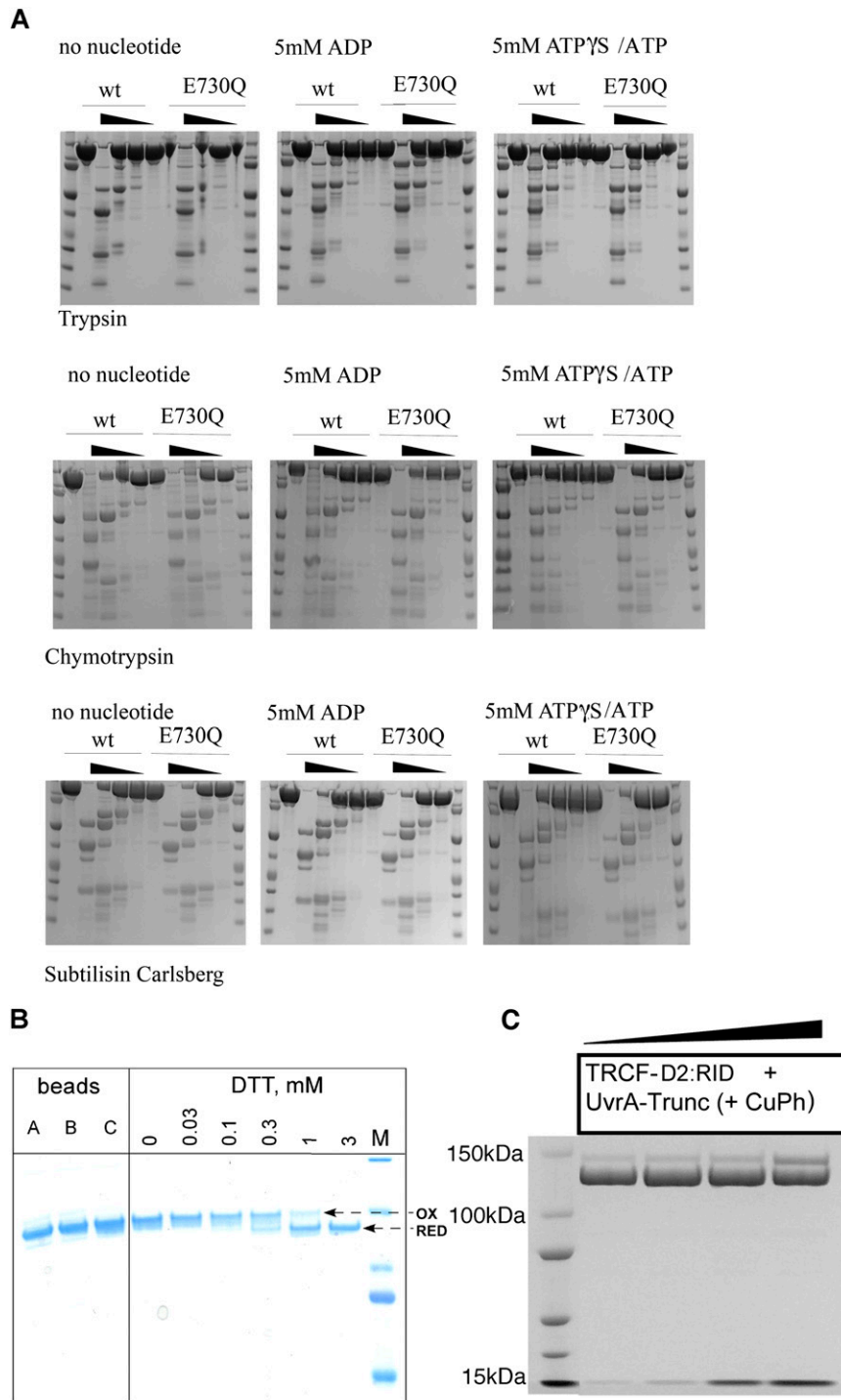

Fig. S3. Limited proteolysis of TRCF and TRCF-E730Q and cross-linking of TRCF variants. (*A*) Digestions were carried out with increasing concentrations of trypsin (*Top*), chymotrypsin (*Middle*), and subtilisin Carlsberg (*Bottom*). (*B*) SDS/PAGE of the TRCF-D2:D7 variant after incubations with the magnetic beads used in RNA-release assays and increasing concentrations of reducing agents. (*C*) SDS/PAGE of TRCF-D2:RID oxidized in the presence of 4 μM Cu(II) (1, 10) phenanthroline (CuPh) and increasing concentrations of UvrA-Trunc.
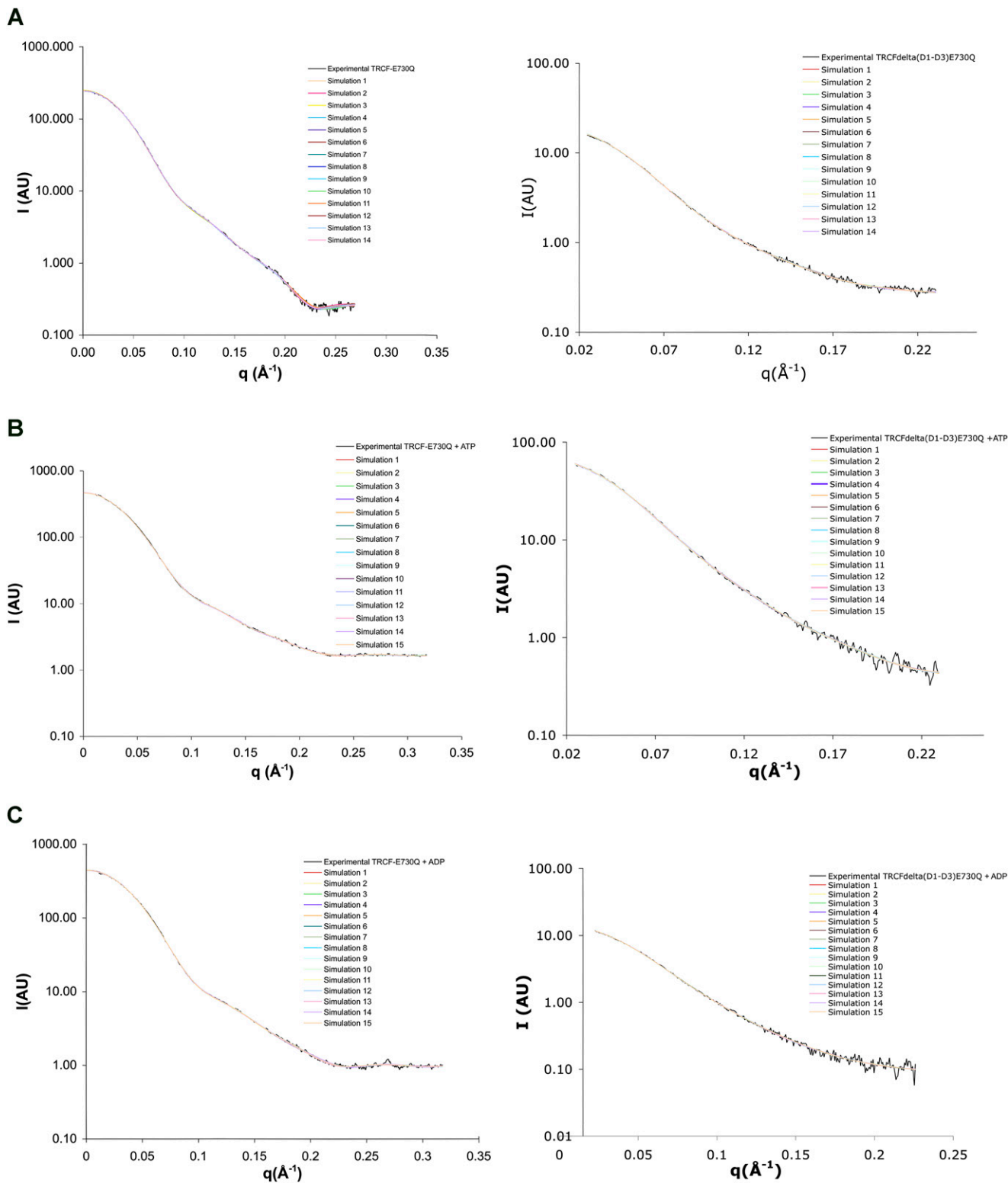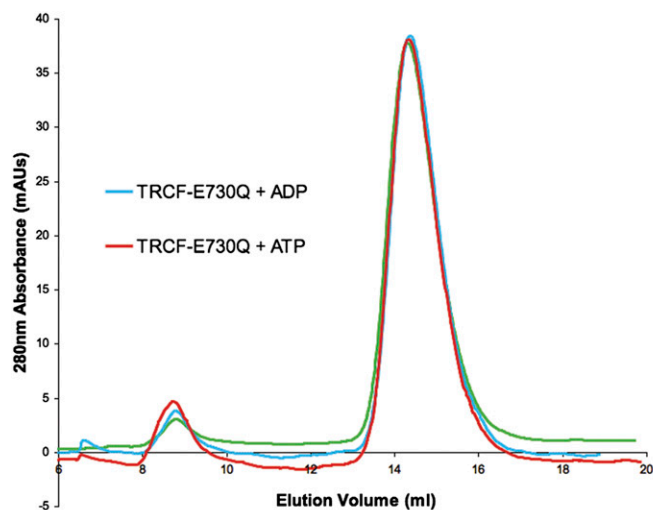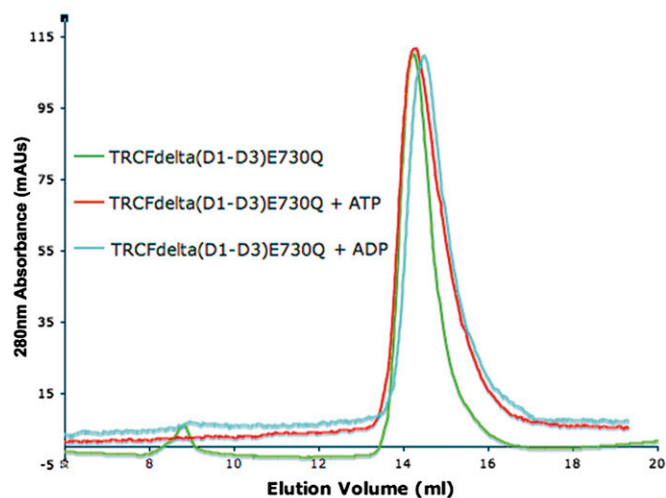
Fig. S4. Comparison between the observed and simulated scattering of the obtained GASBOR dummy residue models obtained in the absence of nucleotide (*A*), with ATP (*B*) and ADP (*C*).

Theoretical Molecular Weight: 130 kDa
Apparent Molecular Weight :
 TRCF-E730Q: 130 kDa
 TRCF-E730Q + ADP: 130 kDa
 TRCF-E730Q + ATP: 130 kDa

Theoretical Molecular Weight: 76 kDa
Apparent Molecular Weight:
 TRCFdelta(D1-D3)E730Q: 73 kDa
 TRCFdelta(D1-D3)E730Q + ADP: 64 kDa
 TRCFdelta(D1-D3)E730Q + ATP: 70 kDa
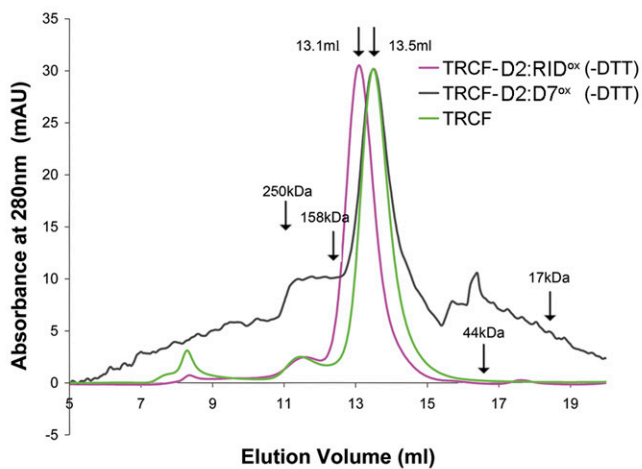
TRCF Apparent Molecular Weight = 124kDa
TRCF-D2:RID^{ox} Apparent Molecular Weight= 148kDa
TRCF-D2:D7^{ox} Apparent Molecular Weight= 124kDa

Fig. S5. Size-exclusion chromatography confirms TRCF variants are monomeric. Curves indicate the elution of TRCF-E730Q and TRCF-E730QΔ(D1-D3)E730Q in the absence of nucleotide (green), with ADP (cyan) or ATP (red). *Lower* panel indicates the elution profile of oxidized TRCF variants, demonstrating the engineered disulfides are intramolecular rather than intermolecular.
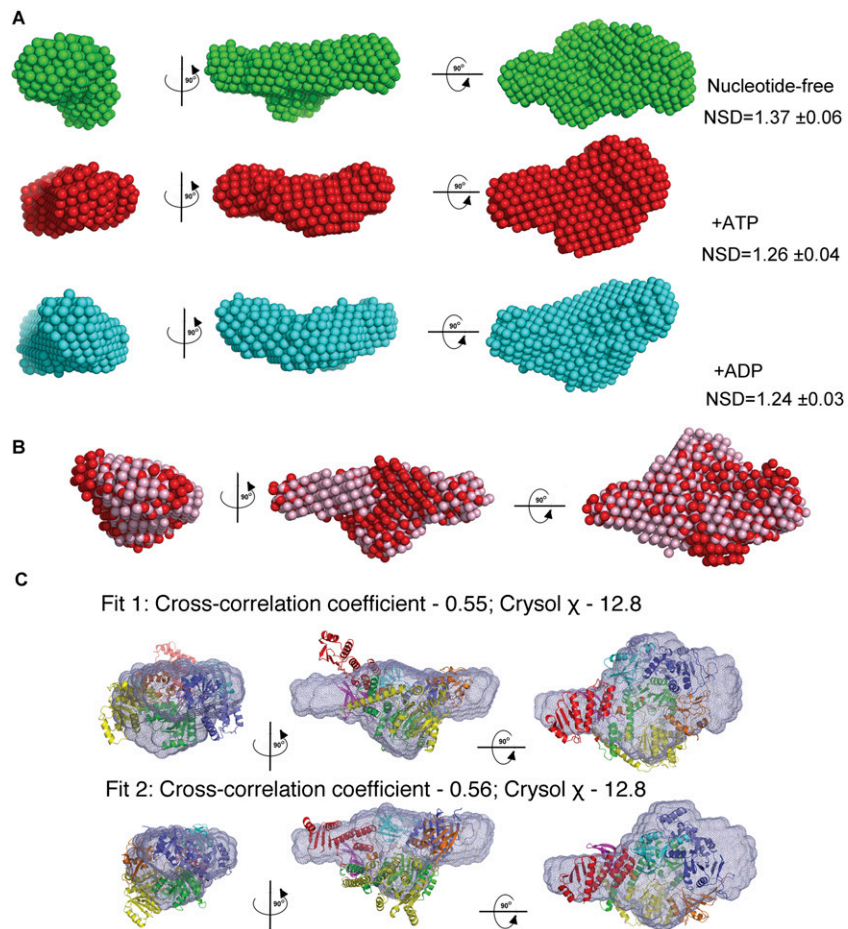
Fig. S6. SAXS bead models. (*A*) Models for the hyperactive variant TRCFΔ(D1-D3)E730Q. (*B*) Ab initio (red) and coordinate-seeded model (pink) for ATP-bound TRCF. Views are as in Fig. 3, and mean NSD values are indicated with SD. (*C*) Rigid-body fitting of the crystallographic model of nucleotide-free TRCF into the SAXS envelopes obtained for the TRCF-E730Q mutant in the presence of ATP. Fitting of the atomic model into the SAXS-derived volumetric map resulted in two possible placements with a similar correlation coefficient. The X-ray TRCF model is color-coded by domain as in Fig. 1, and the SAXS volumetric map is represented as a gray mesh.
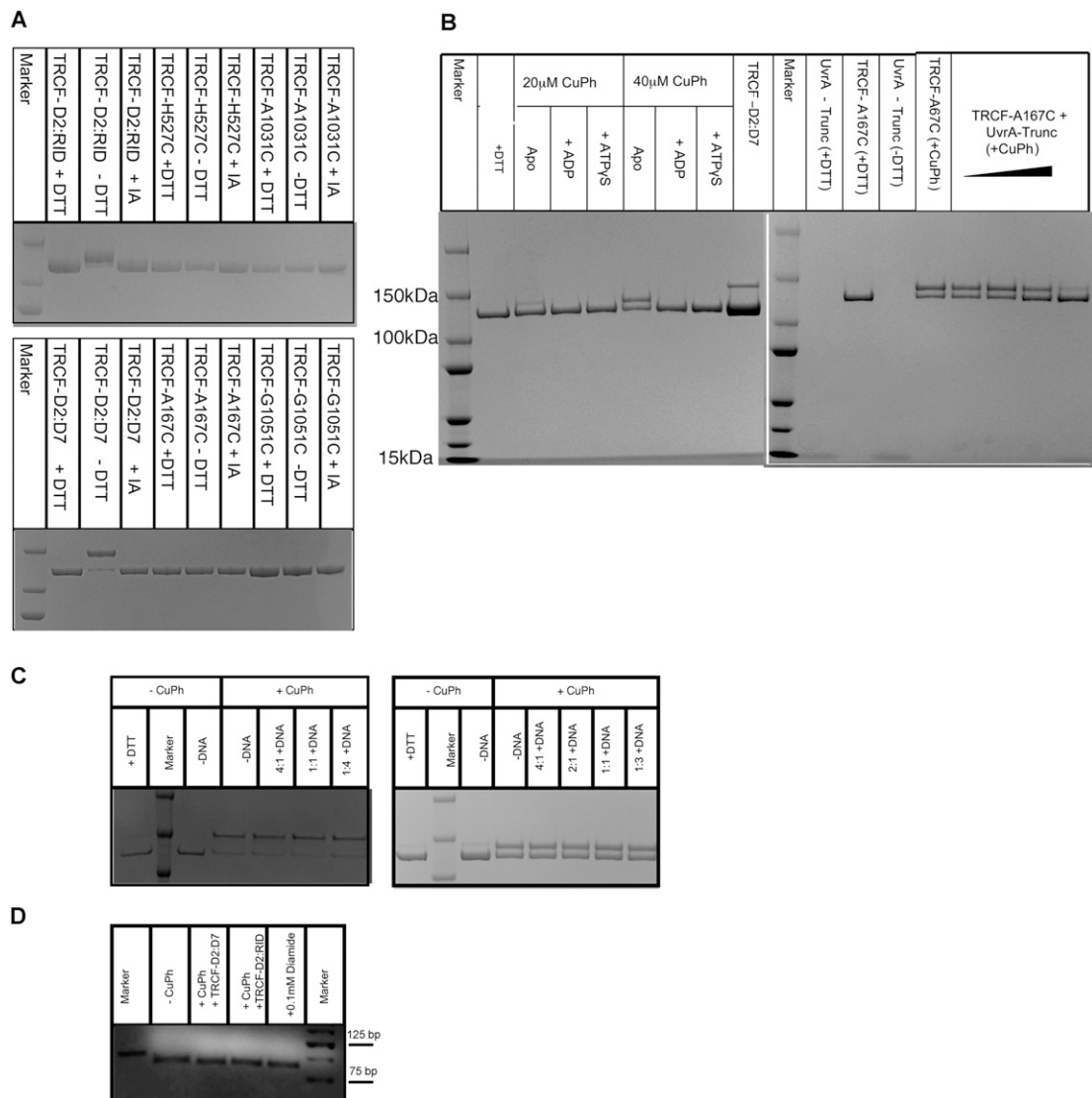
Fig. S7. Electrophoretic analysis of TRCF variants. (*A*) SDS/PAGE of the purified double mutants TRCF-D2:RID and TRCF-D2:D7 and single cysteine mutants in the presence and absence of the reducing agent DTT and the alkylating agent iodoacetamide (IA). (*B*) SDS/PAGE of TRCF-A167C cross-linking reactions in the presence of Cu(II) (1, 10) phenanthroline (CuPh) and nucleotides ADP and ATPγS (*Left*) and various concentrations of weakly staining UvrA-Trunc (*Right*). (*C*) SDS/PAGE of TRCF Cys variants, TRCF-D2:D7 (*Left*) and TRCF-D2:RID (*Right*), oxidized in the presence of CuPh and increasing concentrations of dsDNA. (*D*) Agarose electrophoresis of dsDNA incubated with CuPh (and alternative oxidizing agent diamide) in the absence/presence of TRCF variants.
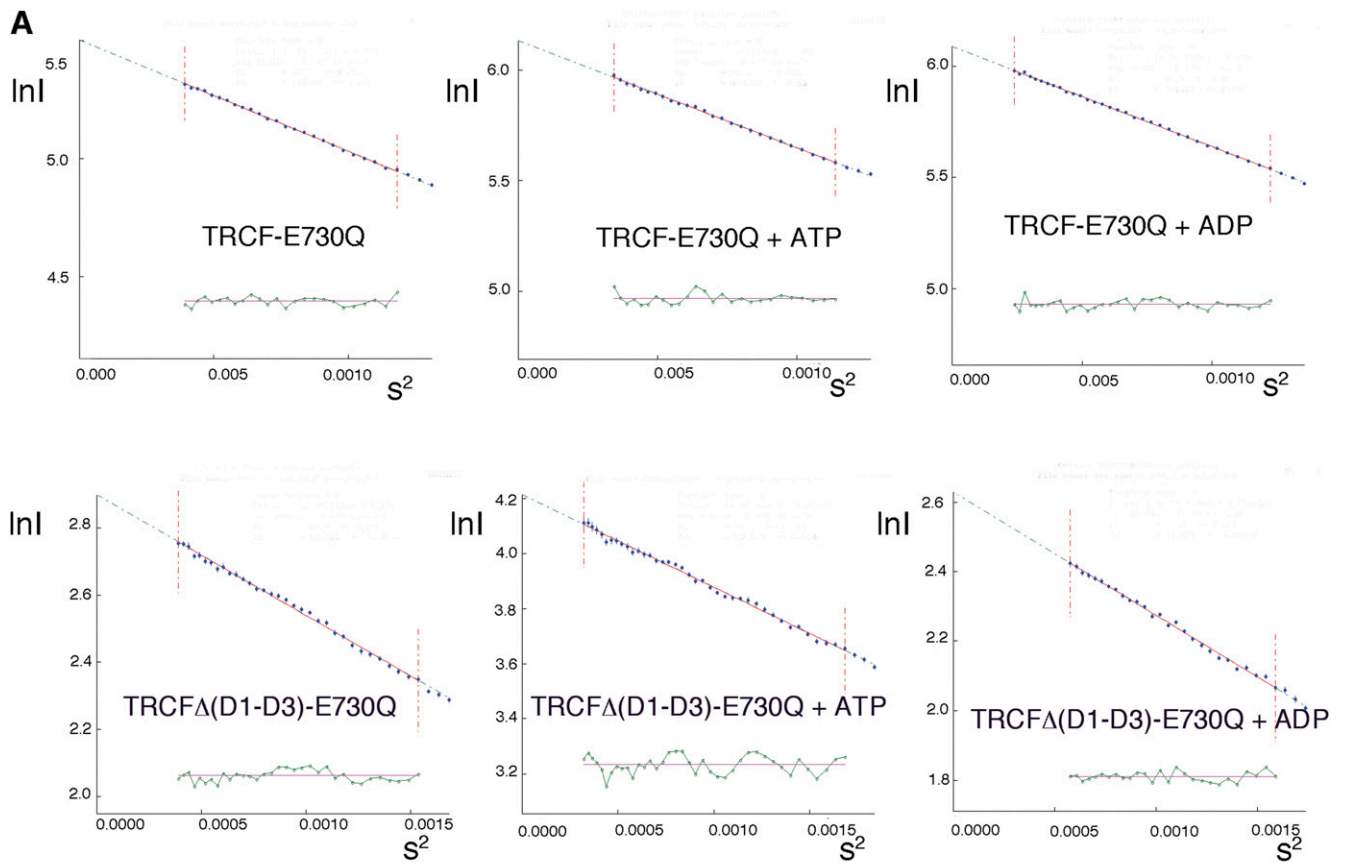
Fig. S8. Guinier analysis and electron density map. (*A*) Guinier plots of SAXS data. Graphical representation of the residuals is shown in light green. (*B*) Stereogram with a representative section of the sigmaA-validated $2|F_o| - |F_c|$ electron density map in the region of the TRCF/UvrA interface. Atomic model is shown in stick representation. The electron density map is contoured at 1.4σ.

Table S1. X-ray intensity and refinement statistics for the _E. coli_ TRCF–Trunc/UvrA–Trunc complex

	TRCF-Trunc/UvrA-Trunc	
Intensity statistics	Dataset 1	Dataset 2
Space group	P6$_2$22	P6$_2$22
Cell dimensions		
a, b, c (Å)	119.1, 119.1, 234.2	119.2, 119.2, 234.3
α, β, γ (°)	90.00, 90.00, 120.00	90.00, 90.00, 120.00
Resolution (Å)	30.0–3.0 (3.1–3.0)*	30.0–2.8 (2.9–2.8)*
No. of reflections	20,398	24,835
R_{merge}	10.8 (64.2)*	7.5 (60.4)*
I/σI	31(2)*	26 (1.7)*
Completeness (%)	99.9 (98.3)*	99.5 (96.0)*
Redundancy	22 (12.4)*	6.4 (4.8)*
Refinement statistics		
Resolution (Å)	30.0–2.8	
No. of reflections (test set)	24,708 (1,240; random 5%)	
R_{work}/R_{free}	23.8/28.2 (41.2/49.2)*	
Cross-validated maximum-likelihood coordinate error (Å)	0.92	
No. of atoms	3,143	
Protein	3,143	
Ligand/ion	—	
Water	—	
B-factors (Å^2)		
Protein, isotropic-equivalent	93	
Ligand/ion	—	
Water	—	
rms deviations		
Bond lengths (Å)	0.008	
Bond angles (°)	1.360	

*Values in parentheses are for highest-resolution shell.

Table S2. SAXS experimental and calculated radii of gyration R_g and maximum intramolecular distance D_{max} for TRCF-E730Q and TRCFΔ(D1-D3)E730Q

	PDB ID 2EYQ	TRCF-E730Q	TRCF-E730Q+ATP	TRCF-E730Q+ADP
$R_{g,\ Experimental,\ Guinier}$ (Å)	—	37.6 ± 0.2	38.1 ± 0.3	36.8 ± 0.1
$R_{g,\ Experimental,\ real-space}$ (Å)	—	37.1 ± 0.1	38.2 ± 0.1	36.6 ± 0.1
$R_{g,\ Calculated}$ (Å)	35.8	—	—	—
$D_{max,\ Experimental}$ (Å)	—	124 ± 5	140 ± 5	126 ± 5
$D_{max,\ Calculated}$ (Å)	113	—		

	PDB ID 2EYQ Δ(D1-D3)	TRCFΔ(D1-D3) E730Q	TRCFΔ(D1-D3) E730Q + ATP	TRCFΔ(D1-D3) E730Q + ADP
$R_{g,\ Experimental,\ Guinier}$ (Å)	—	32.9 ± 0.2	31.8 ± 0.2	32.6 ± 0.2
$R_{g,\ Experimental,\ real-space}$ (Å)	—	34.1 ± 0.1	32.9 ± 0.1	33.3 ± 0.1
$R_{g,\ Calculated}$ (Å)	31.0	—	—	—
$D_{max,\ Experimental}$ (Å)	—	113 ± 5	116 ± 5	115 ± 5
$D_{max,\ Calculated}$ (Å)	102	—	—	—